

SparseCam4D: Spatio-Temporally Consistent 4D Reconstruction from Sparse Cameras

Weihong Pan^{1,2*} Xiaoyu Zhang^{2*} Zhuang Zhang Zhichao Ye² Nan Wang²
 Haomin Liu² Guofeng Zhang^{1,2†}
¹State Key Lab of CAD&CG, Zhejiang University ²InSpatio Research

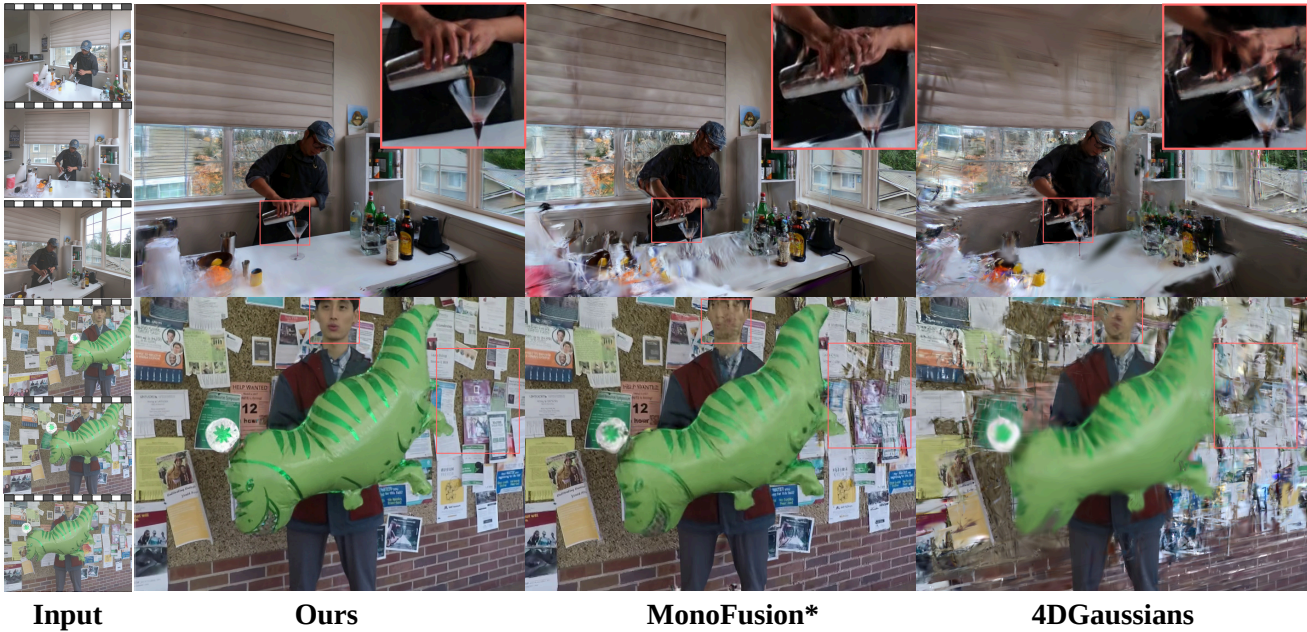


Figure 1. **Novel view rendering comparison.** With as few as 2-3 cameras, our approach reconstructs high-quality dynamic scenes with spatio-temporal consistency and photorealistic quality. Please refer to our project page for additional dynamic results.

Abstract

High-quality 4D reconstruction enables photorealistic and immersive rendering of the dynamic real world. However, unlike static scenes that can be fully captured with a single camera, high-quality dynamic scenes typically require dense arrays of tens or even hundreds of synchronized cameras. Dependence on such costly lab setups severely limits practical scalability. To this end, we propose a sparse-camera dynamic reconstruction framework that exploits abundant yet inconsistent generative observations. Our key innovation is the Spatio-Temporal Distortion Field, which provides a unified mechanism for modeling inconsistencies in generative observations across both spatial and temporal dimensions. Building on this, we de-

velop a complete pipeline that enables 4D reconstruction from sparse and uncalibrated camera inputs. We evaluate our method on multi-camera dynamic scene benchmarks, achieving spatio-temporally consistent high-fidelity renderings and significantly outperforming existing approaches. Project page: <https://inspatio.github.io/sparse-cam4d/>

1. Introduction

Advances in dynamic scene novel view synthesis (NVS), particularly real-time 4D Gaussian Splatting (4DGS), have enabled high-fidelity dynamic rendering and hold great potential for applications in VR/AR, film production, short videos, live streaming, etc. [20, 41].

However, immersive 4D reconstruction generally requires dense camera inputs. Unlike static scenes that can

*Equal contributions.

†Corresponding authors.

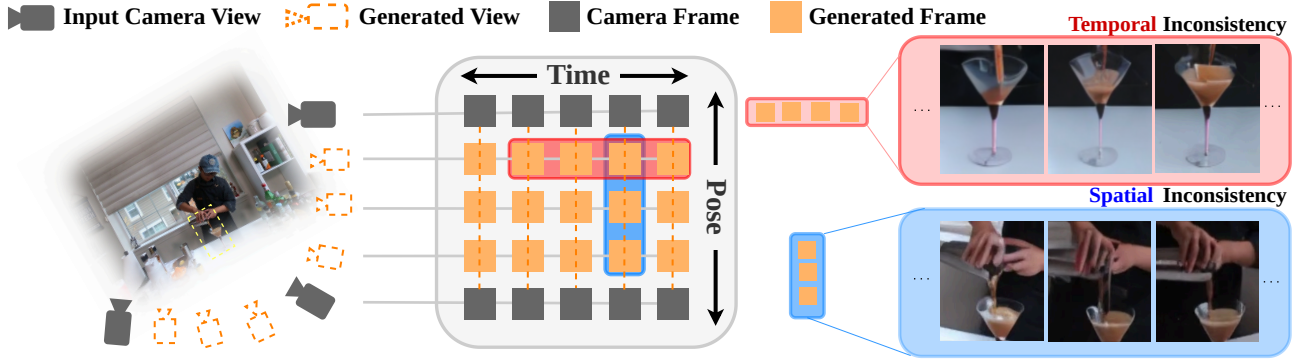


Figure 2. **Spatio-temporal inconsistency.** Real cameras (grey) capture consistent content of multi-view dynamic scene, while generative results (orange) include additional observations at different poses and time. Inconsistencies across poses at the same time are referred to as *spatial inconsistencies*, and inconsistencies across time at the same pose are referred to as *temporal inconsistencies*.

be captured with a single camera, high-quality dynamic scene benchmarks [13, 26, 46] are typically constructed using dense camera arrays comprising approximately 20 synchronized cameras. Such costly lab setups severely hinder broader adoption and scalability.

Therefore, we aim to reconstruct high-fidelity dynamic scenes from sparse cameras. Sparse-view 4D reconstruction remains largely unsolved [47], as spatio-temporally consistent reconstruction of complex motions relies heavily on dense observations. Sparse inputs aggravate the ill-posed nature of 4D reconstruction [10], making this task highly challenging.

Geometric regularization is an intuitive strategy for sparse-view reconstruction [47]. MonoFusion [35], followed with Shape-of-Motion [32], uses depth and tracking regularization to align 4D scene content and improve multi-view consistency in novel view synthesis. However, these regularization techniques mainly focus on structural constraints and are insufficient to preserve accurate appearance, causing the rendering quality to quickly collapse under viewpoint shifts, as shown in Fig. 1, which prevents free-viewpoint exploration.

With the remarkable progress in Camera-Controlled Video Diffusion Models [2, 3, 48], another intuitive direction is to leverage such models to generate high-quality spatio-temporal data, thereby providing additional observation for 4D reconstruction. However, these photorealistic generated results often exhibit spatio-temporal inconsistencies, such as flickering surfaces and unstable object motions across views and time, as shown in Fig. 2, which undermine the coherence of dynamic scenes and cause severe blurring and artifacts.

To this end, our key innovation is the Spatio-Temporal Distortion Field (STDF), a lightweight mechanism enables unified modeling of inconsistencies in generative observations across both space and time. Notably, the STDF is discarded after training, thus introducing zero additional com-

putational overhead to novel view rendering. Moreover, due to the difficulty of obtaining accurate pose priors from sparse inputs, we conduct experiments using uncalibrated sparse views. Our pipeline jointly optimizes pose, rendering, and smoothness terms to produce spatio-temporally consistent dynamic reconstructions.

Finally, we validate our approach on three standard 4D reconstruction benchmarks, including Neural 3D Video [13], Technicolor [26], and Nvidia Dynamic Scenes [46]. To the best of our knowledge, this is the first work to achieve sparse-camera 4D reconstruction on dynamic scene benchmarks, evaluated across all camera views.

Our contributions are as follows: **(i)** We propose unified modeling of spatio-temporal inconsistencies in generative observations by introducing the Spatio-Temporal Distortion Field (STDF). **(ii)** We present a complete pipeline and optimization strategy that supports high-fidelity 4D scene reconstruction from uncalibrated sparse inputs. **(iii)** Through extensive experiments across multi-camera 4D benchmarks, our method demonstrates clear advantages over prior work, delivering photorealistic novel view renderings of dynamic scenes with spatio-temporal consistency under sparse-camera inputs.

2. Related Work

2.1. Sparse-view dynamic reconstruction

Although numerous recent works [4, 7, 11, 13, 14, 16, 38, 43, 44] reconstruct dynamic scenes from densely captured and well-synchronized multi-view video inputs. In contrast, sparse-view dynamic reconstruction is still in its early stages. Some studies have initially focused on reconstructing dynamic content of objects or human bodies using sparse cameras. Works such as [9, 24, 25, 36] build a canonical static 3D space based on SMPL priors and learn a deformation field to map it to Gaussian primitives at different time steps. [10] utilizes existing human

datasets and train a spatio-temporal diffusion model under the guidance of SMPL priors to generate additional temporally consistent multi-view human videos for reconstruction. Research on sparse-view dynamic reconstruction in real-world scenes remains limited. A recent line of work explores dynamic reconstruction from monocular videos [12, 15, 18, 22, 32, 37]. Nevertheless, these approaches are heavily dependent on monocular depth estimation and tracking-based regularization, and without multi-view constraints, the rendering of novel views quickly collapses under viewpoint shifts, making it difficult to obtain roamable, high-quality 4D scenes. MonoFusion [35] improves upon this line by integrating monocular depth, 3D tracking information, and DINOv2 [21] features, extending monocular 4D reconstruction methods to sparse-view settings. Nevertheless, results show that under these geometric regularizations, the rendering quality remains suboptimal, exhibiting floating artifacts, missing details, and geometric distortions, making it challenging to achieve photorealistic renderings in novel view.

2.2. Diffusion Model for Novel View Synthesis.

The rapid progress of video diffusion models (VDMs) has enabled generating continuous videos conditioned on a single image. Within the context of novel view synthesis, several works [17, 19, 29, 39, 45] directly focus on multi-view consistent video generation, but they are mostly constrained to object-centric settings. Scene-level video generation methods [30, 31, 40] attempt to improve consistency via multi-view diffusion models. Yet, limited real-world multi-view video data and the inherent trade-off between spatial accuracy and generative capability lead to frequent inconsistencies, making precise 4D reconstruction in realistic environments highly challenging. Another line of work, camera-controlled video diffusion model, incorporates camera motion control during generation for controllable novel-view videos. [34] introduces a Camera Motion Control Module that injects camera extrinsic parameters into temporal transformers. [3, 8, 42] further improve controllability by replacing explicit camera pose parameters with Plücker ray embeddings. [48] incorporate point cloud priors to improve motion control stability. However, generated frames remain spatially and cross-view inconsistent, limiting their suitability in 4D reconstruction. We address this by enforcing consistency across space, time, and viewpoints.

3. Method

In this section, we introduce a novel framework that harnesses video diffusion models as a source of auxiliary visual observations, facilitating 4D scene reconstruction when only a limited set of input views is available. Sec 3.2 introduces the overall framework. Sec 3.3 details the core com-

ponent - Spatio-Temporal Distortion Field - which helps to incorporate generated images into 4D scene reconstruction. Finally, Sec 3.4 describes the optimization scheme.

3.1. Preliminary

4D Gaussian Splatting. A line of 4DGS approaches directly models Gaussian primitives in 4D space to represent the dynamic scene. In this paradigm, the temporal axis is treated as an additional independent coordinate dimension, such that 3D Gaussians are directly lifted into 4D. Each 4D Gaussian is parameterized by its center position $\boldsymbol{\mu} = (\mu_x, \mu_y, \mu_z, \mu_t)$ and a covariance matrix $\boldsymbol{\Sigma} \in \mathbb{R}^{4 \times 4}$, where $\boldsymbol{\Sigma}$ is decomposed into a scaling matrix $\boldsymbol{S} = \text{diag}(s_x, s_y, s_z, s_t)$ and a rotation matrix $\boldsymbol{R} \in \mathbb{R}^{4 \times 4}$. Same as 3D Gaussians, each 4D primitive maintains a set of SH coefficients and an opacity α .

To parameterize 4D rotation matrix in Euclidean space, algebraic geometry tools such as pair of isotropic rotations [43] $\boldsymbol{R} = L(\boldsymbol{q}_l)R(\boldsymbol{q}_r)$ or a normalized 4D rotor \mathbf{r} with 8 coefficients [5] $\boldsymbol{R} = \mathcal{F}_{map}(\mathcal{F}_{norm}(\mathbf{r}))$ are employed, which are mathematically equivalent. At a given timestamp t , temporal slicing is performed to project the attributes of each 4D Gaussian into the corresponding 3D subspace as follows [5]:

$$\mathcal{G}_{3D}(\mathbf{x}, t) = e^{-\frac{1}{2}\lambda(t-\mu_t)^2} e^{-\frac{1}{2}[\mathbf{x}-\boldsymbol{\mu}(t)]^T \boldsymbol{\Sigma}_{3D}^{-1}[\mathbf{x}-\boldsymbol{\mu}(t)]}, \quad (1)$$

The rendering process follows the standard differential splatting procedure of 3DGS, while the densification is performed in both spatial and temporal dimensions.

K-planes Factorization. K-planes [7] introduces a simple and interpretable representation for arbitrary d -dimensional scenes, referred to as *K-planes factorization*. In this framework, $k = \binom{d}{2}$ planes are employed to represent every combinations of two dimensions. Taking an d -dimensional coordinate as input, K-planes maps it to a feature vector, which is then decoded by a tiny MLP to obtain target attribute value. For dynamic 4D scenes, this results in the so-called *hex-planes*, consisting of three space-only planes xy , xz , yz and three space-time planes xt , yt , zt . Such a representation has been widely adopted in both deformation-based NeRF and 4DGS methods. NeRFs use it to estimate a world-to-canonical mapping [7] $\mathcal{M} : (\mathbf{p}, t) \rightarrow \Delta\mathbf{p}$, where \mathbf{p} reveals to the world spatial point and t is the target time. Then the vanilla NeRF pipeline is applied with canonical spatial point $\mathbf{p} + \Delta\mathbf{p}$ and view direction \mathbf{d} as input. 4DGS using it to compute the canonical-to-world mapping [38] $\mathcal{F} : (\mathcal{G}, t) \rightarrow \Delta\mathcal{G}$ for each attribute of a canonical 3D Gaussian primitive \mathcal{G} at time t . An image I with view matrix $\mathbf{M} = [\mathbf{R}|\mathbf{T}]$ is rendered by the differential splatting with the deformed 3D Gaussians \mathcal{G}' following $I = \mathcal{S}(\mathbf{M}, \mathcal{G}')$, where $\mathcal{G}' = \mathcal{G} + \Delta\mathcal{G}$.

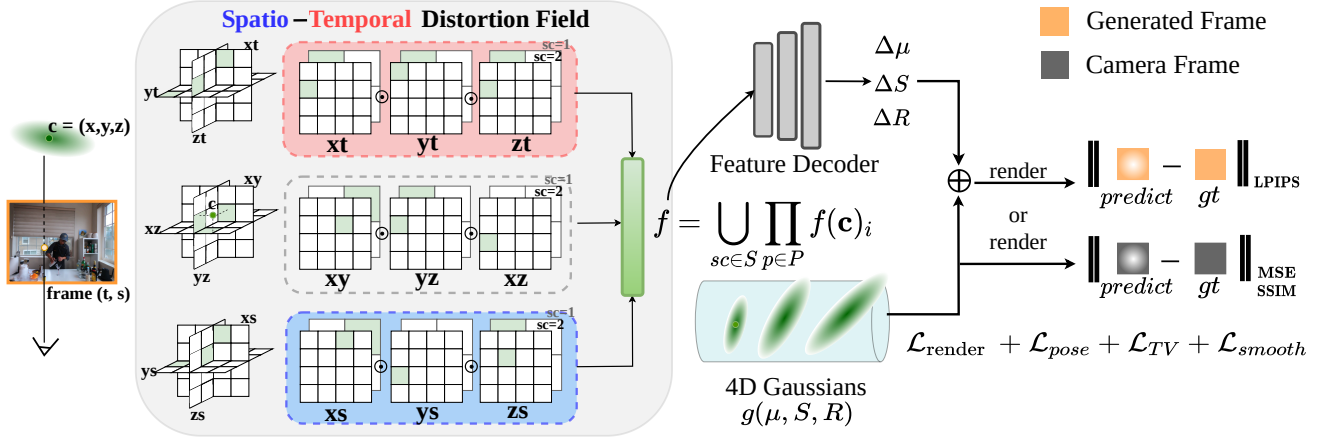


Figure 3. **Method overview.** Given a generated frame at temporal index t and pose index s , each 4D Gaussian at $c = (x, y, z)$ is projected onto the planes of the Spatio-Temporal Distortion Field to obtain deformation features, which are then decoded by a small MLP to produce the deformation values. We use separate photometric losses for real and generated frames, and additionally introduce regularization terms on pose, feature plane, and spatial smoothness to enhance optimization stability.

3.2. Framework

Given N sparse input camera videos with L frames, our goal is to optimize a 4DGS model using auxiliary generated sequences. For simplicity, we refer to the set of images from N input video sequences and their corresponding camera poses as *input views* $V_I = \{(I_s^t, [\mathbf{R}|\mathbf{T}]_s) | t = 0, \dots, L; s = 0, \dots, N\}$, and the set of images I from M generated video sequences with their poses $[\mathbf{R}|\mathbf{T}]$ as *generated views* $V_G = \{(I_s^t, [\mathbf{R}|\mathbf{T}]_s) | t = 0, \dots, L; s = 0, \dots, M\}$. The 4DGS model is trained with $V_I + V_G$.

The noising and denoising process of video diffusion models introduces severe geometric inconsistencies across space and time during generation. If such generated views are directly used for scene reconstruction, these inconsistencies will significantly degrade the geometric consistency of 4DGS, leading to noticeable artifacts. Therefore, when leveraging such diffusion-based observations to assist reconstruction, it is crucial to extract and disentangle these inconsistencies to construct canonical 4D Gaussians.

Our framework consists of 4D Gaussians \mathcal{G}_{4D} and a spatio-temporal distortion field \mathcal{F} that models the inconsistencies in each generated view $V_G^{t,s} \in V_G$, formally represented as:

$$\mathcal{F} : (\mathcal{G}_{4D}, t, s) \rightarrow \Delta\mathcal{G}_{4D}. \quad (2)$$

where t denotes the time index, while s denotes the pose index, as illustrated in Fig. 2. Through the proposed distortion field, the variation of canonical 4D Gaussians on a generated view can be obtained, which then yields the distorted 4D Gaussians $\mathcal{G}'_{4D} = \mathcal{G}_{4D} + \Delta\mathcal{G}_{4D}$. For a generated view indexed by (t, s) , our framework converts the canonical 4D Gaussians to a set of distorted Gaussians while preserving compatibility with differentiable splatting.

3.3. Spatio-Temporal Distortion Field

Specifically, the spatio-temporal distortion field \mathcal{F} consists of an Ennea-plane representation and a lightweight multi-head MLP serving as the fused feature decoder. We factorize the 5D volume defined by (x, y, z, t, s) into $k = \binom{5}{2} = 10$ two-dimensional planes, each corresponding to a pair of dimensions. Since the combination (t, s) does not encode any form of distortion, this plane is omitted. Consequently, such factorization decomposes the 5D neural voxel into nine multi-resolution 2D feature planes $\mathbf{P} = \{\mathbf{P}_{xy}, \mathbf{P}_{xz}, \mathbf{P}_{yz}, \mathbf{P}_{xt}, \mathbf{P}_{yt}, \mathbf{P}_{zt}, \mathbf{P}_{xs}, \mathbf{P}_{ys}, \mathbf{P}_{zs}\}$. Each feature plane is defined as $\mathbf{P}_{ij} \in \mathbb{R}^{lN_i \times lN_j \times h}$, where h denotes the feature dimension, N_i and N_j represent the basis resolution of the corresponding two axes, and l is the scale factor for multi-resolution structure.

Given a 5D coordinate $c = \{x, y, z, t, s\}$, the corresponding feature vector is obtained as follows. First, each dimension of c is normalized to its resolution range $[0, N_i)$, and then coordinate c is projected onto the nine planes aforementioned. The feature of c on each plane is extracted via bilinear interpolation, formally:

$$\begin{aligned} \mathbf{f}(c)_c &= \text{interp}(\mathbf{P}_c, \pi_c(c)), \\ c &\in \{xy, xz, yz, xt, yt, zt, xs, ys, zs\} \end{aligned} \quad (3)$$

where π_c denotes the projection of c onto the corresponding plane, and ‘interp’ indicates the bilinear interpolation over the 2D grid. The features extracted from the feature planes are then fused by element-wise multiplication to obtain an h -dimensional feature vector at a given resolution. Features across different resolutions are then concatenated to form the final features.

$$\mathbf{f}(c) = \bigcup_{sc} \prod_{\mathbf{P}_c \in \mathbf{P}} \mathbf{f}(c)_c \quad (4)$$

These features are decoded by a multi-head MLP decoder $\mathcal{D} = \{\phi, \phi_p, \phi_{q_l}, \phi_{q_r}, \phi_s\}$ into the distortion of various 4D Gaussian attributes, including position $\Delta\boldsymbol{\mu} = \phi_{\boldsymbol{\mu}}(\phi(\mathbf{f}))$, rotation $\Delta\mathbf{q}_l = \phi_{q_l}(\phi(\mathbf{f}))$, $\Delta\mathbf{q}_r = \phi_{q_r}(\phi(\mathbf{f}))$, and scaling $\Delta\mathbf{s} = \phi_s(\phi(\mathbf{f}))$. Then, the distorted attributes can be computed as:

$$(\boldsymbol{\mu}', \mathbf{q}'_l, \mathbf{q}'_r, \mathbf{s}') = (\boldsymbol{\mu} + \Delta\boldsymbol{\mu}, \mathbf{q}_l + \Delta\mathbf{q}_l, \mathbf{q}_r + \Delta\mathbf{q}_r, \mathbf{s} + \Delta\mathbf{s}) \quad (5)$$

During training, the distorted Gaussians are used to render the generated views, while the original Gaussians are used to render the real views. After training, the distortion terms are discarded, and only the canonical 4D Gaussian is retained.

3.4. Optimization

Pose Optimization. Because of the inconsistencies present in the generated video frames, the alignment accuracy is compromised when using traditional COLMAP [27, 28] for estimating camera extrinsics. To mitigate this issue, we propose simultaneous optimization of camera extrinsics along with the 4D Gaussian attributes, treating camera extrinsics as learnable variables likewise.

Loss Function. For input views, we apply the standard photometric loss. The photometric loss includes an \mathcal{L}_1 RGB loss and a D-SSIM loss [33].

$$\mathcal{L}_{\text{input}} = (1 - \lambda)\mathcal{L}_1 + \lambda\mathcal{L}_{\text{D-SSIM}}. \quad (6)$$

For generated views, applying standard photometric loss directly leads to degraded reconstruction quality due to the inherent distortions in generated frames. To address this, we incorporate perceptual loss [49] to supervise texture and reconstruction similarity.

$$\mathcal{L}_{\text{gen}} = \lambda_1\mathcal{L}_1 + \lambda_2\mathcal{L}_{\text{ipips}}. \quad (7)$$

In order to prevent the optimized pose from deviating significantly from their original initialization, a regularization term is introduced:

$$\mathcal{L}_{\text{pose}} = \lambda_p(\|\mathbf{T} - \hat{\mathbf{T}}\| + \|\mathbf{q} - \hat{\mathbf{q}}\|), \quad (8)$$

where \mathbf{T} and \mathbf{q} represent the optimized translation and rotation of a camera, $\hat{\mathbf{T}}$ and $\hat{\mathbf{q}}$ are the corresponding initial extrinsics obtained from COLMAP [27, 28], and parameter λ_p balances the camera optimization term with other loss components.

Additionally, following K-Planes [7], a grid-based total variation loss \mathcal{L}_{TV} is also applied for spatial smoothness. Since the distortions in the generated images from Yu et al. [48] are continuous along the pose axis but exhibit abrupt changes along the time axis, we apply a smoothness regu-

larization over pose axis with a second derivative filter:

$$\begin{aligned} \mathcal{L}_{\text{smooth}} &= \lambda_s \frac{1}{|C|} \sum_{c \in C} \frac{1}{N_i N_s} \sum_{i,s} \|(\mathbf{P}_c^{i,s-1} - \mathbf{P}_c^{i,s}) \\ &\quad - (\mathbf{P}_c^{i,s} - \mathbf{P}_c^{i,s+1})\|_2^2, \quad (9) \\ C &= \{x_s, y_s, z_s\}. \end{aligned}$$

where i, s are indices on plane \mathbf{P}_c , N_i and N_s represent the resolution of each axis. Overall, the total loss can be formulated as:

$$\mathcal{L} = \mathcal{L}_{\text{input}} + \mathcal{L}_{\text{gen}} + \mathcal{L}_{\text{pose}} + \mathcal{L}_{\text{TV}} + \mathcal{L}_{\text{smooth}} \quad (10)$$

4. Experiments

4.1. Experimental Setups

4.1.1. Datasets.

We conduct extensive experiments on three real-world datasets: Neural 3D Video, Technicolor, and Nvidia Dynamic Scenes. Training is performed on two or three selected views that adequately cover the scene content, and evaluation is carried out on **all the remaining views**. For more experimental setting details, please refer to the supplementary material.

Neural 3D Video Dataset. [13] This dataset comprises six indoor multi-view video sequences, recorded simultaneously by 18-21 synchronized cameras at a resolution of 2704×2028 and 30 fps. Following [43], we perform both training and evaluation on downsampled videos by a factor of two, using 300 frames per scene.

Technicolor Dataset. [26] This dataset includes five indoor multi-video sequences acquired with a 4×4 synchronized camera array at a resolution of 2048×1088 . Following [1], we conduct both training and evaluation at full resolution, using 50 frames per scene.

Nvidia Dynamic Scenes Dataset. [46] This dataset contains six outdoor multi-view video sequences, each captured by 12 synchronized cameras at 1920×1080 and 60Hz. We use half-resolution frames and 100 frames per scene for training and evaluation.

4.1.2. Implementation Details.

Our framework is implemented with Pytorch [23] and optimized for 30,000 iterations per scene. At each iteration, one input-view image and one generated-view image are randomly sampled. The first 3000 iterations are trained with a vanilla setting as a warm-up stage, followed by training with both camera optimization and the distortion field, where camera optimization is stopped after 7000 iterations. For generated views, we employ a camera-controlled image-to-video diffusion model [48] which generates $L = 25$ frames per sequence. For uncalibrated generated views and cameras, we obtain coarse pose and point cloud initialization

Table 1. **Qualitative comparisons on Technicolor [26], Neural 3D Video [13], and Nvidia Dynamic Scenes [46] Datasets.** The first and second best performances are highlighted in red and yellow. Our method shows superior performance compared to all baseline methods across all metrics. Note that MonoFusion* is our reproduced version.

Method	Technicolor			Neural 3D Video			Nvidia Dynamic Scenes		
	PSNR \uparrow	SSIM \uparrow	LPIPS \downarrow	PSNR \uparrow	SSIM \uparrow	LPIPS \downarrow	PSNR \uparrow	SSIM \uparrow	LPIPS \downarrow
HyperReel [1]	14.14	0.453	0.616	15.63	0.582	0.500	19.88	0.528	0.396
4DGaussians [38]	16.20	0.505	0.552	17.40	0.673	0.320	16.81	0.372	0.516
4D-Rotor [5]	14.85	0.426	0.581	18.20	0.708	0.357	19.38	0.508	0.389
RealTime4DGS [43]	16.53	0.510	0.542	17.31	0.649	0.442	17.91	0.479	0.426
MonoFusion* [35]	17.97	0.578	0.352	18.43	0.738	0.270	20.22	0.590	0.192
Ours	23.15	0.728	0.299	21.91	0.789	0.258	24.81	0.794	0.150

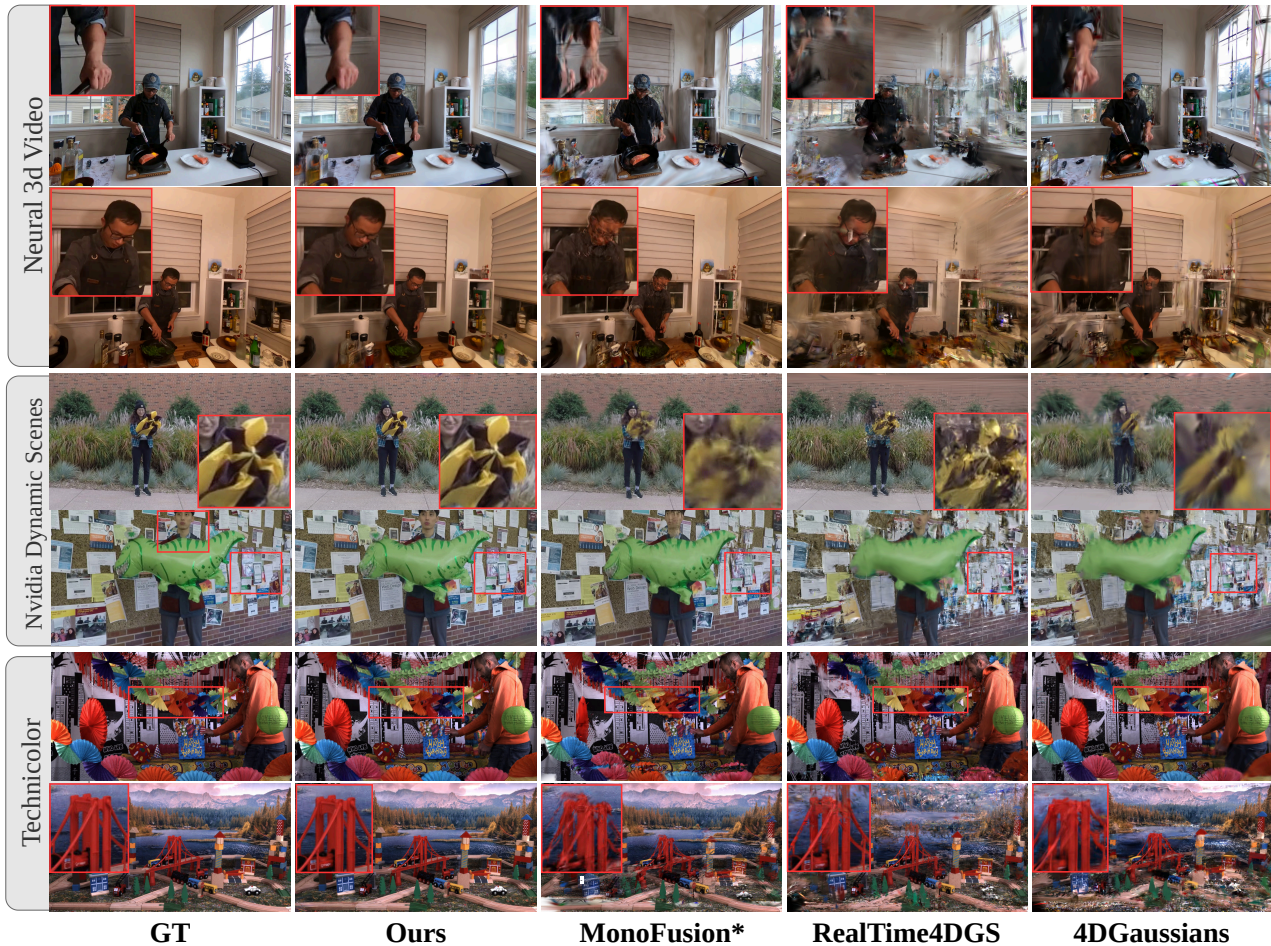


Figure 4. **Qualitative Comparisons of different methods on Technicolor [26], Neural 3D Video [13], and Nvidia Dynamic Scenes [46] Datasets.** We conduct comparisons with representative dynamic scene reconstruction methods: MonoFusion [35], 4DGS [38], 4D-Rotor [5], and Realtime4DGS [43]. MonoFusion* is our reproduced version. Our method significantly outperforms other baselines, producing visually reliable results with sharper details. Please zoom in for more details. Additional qualitative comparisons are included in the supplementary material.

using COLMAP [27, 28] at $t = 0$. The weighting factors λ , λ_1 , λ_2 , λ_p and λ_s are set to 0.2, 0.02, 0.2, 0.1 and 10^{-4} , respectively. All experiments are conducted on a sin-

gle Nvidia A800 GPU to ensure fair comparisons.

Aligning camera poses on test views. In standard 4DGS reconstruction process, the exact camera poses of the test

Table 2. **Ablation studies on STDF.** We randomly select one representative scene from Technicolor [26] and Nvidia Dynamic Scenes [46] to ablate Spatio-Temporal Distortion Field.

Setting	Train		Jumping	
	LPIPS↓	SSIM↑	LPIPS↓	SSIM↑
w/o distortion field	0.608	0.426	0.319	0.674
w/o time axis	0.458	0.480	0.279	0.738
w/o pose axis	0.469	0.462	0.268	0.733
Ours	0.264	0.656	0.170	0.793

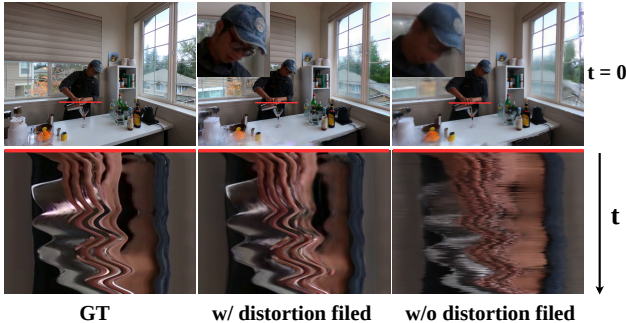


Figure 5. **Spatio-Temporal Consistency.** Rendering results (top) and space-time slices (bottom) constructed by concatenating the red pixel locations across all time steps, demonstrate that direct reconstruction from diffusion observations leads to severe blur and temporal instability (e.g., the moving hand at the bottom right).

views are usually available, as they can be estimated together with the training views under a shared coordinate system before reconstruction. However, in our experimental setting, the poses of test views are unknown and pose optimization is applied during training. Therefore, aligning test-view poses before rendering is essential. Following the protocol of [6], the trained 4DGS is kept fixed while only the test-view poses are refined. This optimization minimizes the l_1 photometric loss between rendered and ground-truth images, yielding more accurate alignment of the rendered results with test views. Such alignment eliminates errors caused by inaccurate poses, ensuring a fairer comparison.

4.2. Results of Dynamic Novel View Synthesis

We adopt PSNR, SSIM [33], and LPIPS [49] as evaluation metrics for comparing the rendering quality of our method against baselines. As the compared baselines do not include pose optimization, we adopt the ground-truth poses for both training and rendering. While this setup provides the baselines with a mild advantage, it does not overcome the fundamental challenge caused by sparse camera inputs. Qualitative and quantitative results are shown in Fig. 4 and Tab. 1, respectively. The visualization results and metrics demonstrate that our approach consistently produces sharper details, more stable dynamics, and fewer artifacts under sparse-camera settings, achieving substantially

better visual quality and spatio-temporal consistency than all baseline methods. For general 4DGS methods such as 4DGaussians [38] and RealTime4DGS [43], their performance drops significantly due to the ill-posed nature of sparse-camera condition, producing broken geometry, noisy renderings and missing details in dynamic regions. These results highlight their reliance on dense and well-aligned inputs. Compared with general 4DGS, MonoFusion [35] benefits from various geometric priors and thus offers relatively high-quality initialization. This leads to noticeable improvements in static background regions. However, it still produces artifacts and geometric misalignments, especially in complex dynamic regions. For instance, in the Nvidia Dynamic Scenes dataset, rapid motions and occlusions cause its priors to fail to capture fine-grained dynamics, resulting in unreliable constraints and degraded reconstructions. The limitation mainly stems from the insufficient quality and robustness of the imposed priors under highly dynamic settings. In contrast, our method leverages generative priors and explicitly disentangles distortions using the proposed spatio-temporal distortion field, achieving spatio-temporal consistency even under challenging conditions, including large view ranges and complex foreground dynamics. For example, in the Neural 3D Video dataset, our method reconstructs both static and dynamic regions with fine-grained details, while in the Nvidia Dynamic Scenes dataset, it preserves temporal stability despite outdoor motions. These results demonstrate that our method not only mitigates artifacts and geometric failures observed in baselines but also provides robust and reliable reconstructions across diverse datasets.

4.3. Ablation and Analysis

LPIPS and SSIM are adopted for ablation, as these two metrics better capture structural similarity and detail fidelity and reflect the impact of each component more accurately. Further details are provided in the supplementary material.

Effectiveness of the Spatio-Temporal Distortion Field.

The ‘w/o distortion field’ variant removes the proposed Spatio-Temporal Distortion Field and directly reconstructs 4D scenes with generated images. As shown in Tab. 2 and Fig. 5, it produces severe blur result due to the spatio-temporal inconsistencies introduced by generative observations, whereas our distortion field substantially mitigates such problem and significantly improves rendering quality. The space-time slice depicted in Fig. 5 (bottom) is obtained by concatenating the red pixels on Fig. 5 (top) across all time steps. Compared with reconstructing directly with generated images, our method yields more temporally coherent outputs that closely match the ground-truth motion, validating the effectiveness of the proposed distortion-aware 4DGS design.

In addition, to further validate the effectiveness of STDF

Table 3. **Ablation studies on pose optimization and loss components.** We randomly select one representative scene from Technicolor [26] and Nvidia Dynamic Scenes [46] Datasets to ablate pose optimization and loss components.

Setting	Train		Jumping	
	LPIPS↓	SSIM↑	LPIPS↓	SSIM↑
w/o pose optimization	0.336	0.569	0.217	0.754
w/o \mathcal{L}_{lrips}	0.285	0.646	0.185	0.782
w/o \mathcal{L}_{TV}	0.309	0.616	0.191	0.768
w/o \mathcal{L}_{smooth}	0.308	0.619	0.191	0.770
Ours	0.264	0.656	0.170	0.793

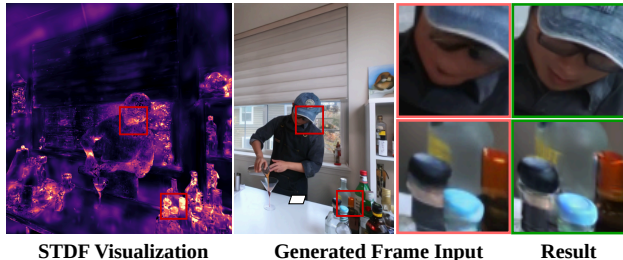


Figure 6. **Visualization of the STDF.** Spatio-Temporal Distortion Field output is rendered as a per-primitive attribute, with brighter regions indicating higher distortions (left). The corresponding areas in the input generated image (right) align with regions exhibiting noticeable deformation (red box).

for jointly capturing spatial and temporal inconsistencies, we conducted the following two experiments. The ‘w/o temporal index’ and ‘w/o pose index’ variants remove the t -axis and s -axis in the STDF respectively, thereby modeling inconsistencies only along spatial or temporal dimensions. As shown in Tab. 2, the noticeable performance degradation indicates that generative inconsistencies manifest across both space and time. This validates the necessity of our two-dimensional temporal design, which more effectively aligns spatio-temporal content and improves rendering quality.

Effectiveness of Pose Optimization. In the *w/o pose optimization* variant, camera poses are fixed during training without refinement. As reported in Tab. 3, incorporating pose optimization substantially enhances reconstruction quality. This demonstrates that generative distortions can severely bias pose estimation, and correcting them during training is necessary for consistent 4D reconstruction.

Ablation on Spatio-Temporal Regularization. We employ \mathcal{L}_{tv} on spatial planes and \mathcal{L}_{smooth} over pose axis to enforce smoothness constraints. Results in Tab. 3 demonstrate that both terms are necessary for reconstructing high-quality 4D scenes. They reflect the continuity in spatio-temporal distortions, consistent with the gradual deformations observed in diffusion-generated outputs.

Visualization of the Spatio-Temporal Distortion Field. We visualize the STDF output as a per-primitive attribute and render it with alpha-blending, as depicted in Fig. 6

Table 4. **Ablation study with alternative video diffusion models (VDMs) on Cook Spinach.**

Cook Spinach	PSNR↑	SSIM↑	LPIPS↓
ViewCrafter (w/o STDF)	21.42	0.775	0.302
ViewCrafter (w STDF)	23.93	0.832	0.232
ReCamMaster (w/o STDF)	21.97	0.756	0.315
ReCamMaster (w STDF)	23.61	0.806	0.247



Figure 7. **Spatio-Temporal consistency on ReCamMaster.**

(left). Heatmaps highlight regions with pronounced distortions in the generated observations, such as facial features and the wine bottle. This illustrates that, in the diffusion-generated observations along the trajectory, different contents undergo varying degrees of distortion, which relates to how the diffusion model perceives the physical world. After training, our method restores these regions in the GS rendering, demonstrating effective correction of spatio-temporal distortions (Fig. 6 (right)). For additional STDF visualization results, please refer to the supplementary material.

Generality Across Different Video Diffusion Models. As discussed earlier, inconsistencies in generated frames are inherent to existing VDMs. To further validate the applicability of our approach, we conduct experiment on another state-of-the-art camera-controlled VDM, *i.e.*, ReCamMaster [3]. As shown in Tab. 4, neither ViewCrafter nor ReCamMaster is able to directly reconstruct photorealistic 4D scenes, highlighting that inconsistencies in VDM-generated frames severely hinder the convergence of 4D content. In contrast, our method achieves significant improvements. When using ViewCrafter as the generative prior, our pipeline yields an increase of 2.51dB in PSNR, and when using ReCamMaster, a similar gain of 1.76db in PSNR is observed. These results demonstrate the capability of our approach to ensure spatio-temporal consistency even when conditioned on different generative models.

5. Conclusion

We propose a framework that leverages generative models for dynamic scene reconstruction from sparse cameras. We identify spatio-temporal inconsistencies in generative observations as the main barrier to achieving high-quality reconstruction. To address this, we introduce the Spatio-Temporal Distortion Field, explicitly modeling these inconsistencies across both space and time, and integrate it into a unified framework jointly optimizing pose, rendering, and

smoothness for stable convergence. Both the main experiments and ablation studies confirm the advantage of our approach and highlight the critical role of unified spatio-temporal modeling. To the best of our knowledge, this is the first sparse-camera 4D reconstruction method thoroughly evaluated on standard multi-camera dynamic scene benchmarks, enabling widely accessible immersive 4D reconstruction.

Acknowledgment: This work was partially supported by NSF of China (No. 62425209).

References

- [1] Benjamin Attal, Jia-Bin Huang, Christian Richardt, Michael Zollhoefer, Johannes Kopf, Matthew O’Toole, and Changil Kim. Hyperreel: High-fidelity 6-dof video with ray-conditioned sampling. In *Proceedings of the IEEE/CVF Conference on Computer Vision and Pattern Recognition*, pages 16610–16620, 2023. 5, 6
- [2] Sherwin Bahmani, Ivan Skorokhodov, Guocheng Qian, Aleksandr Siarohin, Willi Menapace, Andrea Tagliasacchi, David B Lindell, and Sergey Tulyakov. Ac3d: Analyzing and improving 3d camera control in video diffusion transformers. In *Proceedings of the Computer Vision and Pattern Recognition Conference*, pages 22875–22889, 2025. 2
- [3] Jianhong Bai, Menghan Xia, Xiao Fu, Xintao Wang, Lianrui Mu, Jinwen Cao, Zuozhu Liu, Haoji Hu, Xiang Bai, Pengfei Wan, et al. Recammaster: Camera-controlled generative rendering from a single video. *arXiv preprint arXiv:2503.11647*, 2025. 2, 3, 8
- [4] Ang Cao and Justin Johnson. Hexplane: A fast representation for dynamic scenes. In *Proceedings of the IEEE/CVF Conference on Computer Vision and Pattern Recognition*, pages 130–141, 2023. 2
- [5] Yuanxing Duan, Fangyin Wei, Qiyu Dai, Yuhang He, Wenzheng Chen, and Baoquan Chen. 4d-rotor gaussian splatting: towards efficient novel view synthesis for dynamic scenes. In *ACM SIGGRAPH 2024 Conference Papers*, pages 1–11, 2024. 3, 6
- [6] Zhiwen Fan, Wenyan Cong, Kairun Wen, Kevin Wang, Jian Zhang, Xinghao Ding, Danfei Xu, Boris Ivanovic, Marco Pavone, Georgios Pavlakos, et al. Instantsplat: Unbounded sparse-view pose-free gaussian splatting in 40 seconds. *arXiv preprint arXiv:2403.20309*, 2(3):4, 2024. 7
- [7] Sara Fridovich-Keil, Giacomo Meanti, Frederik Rahbæk Warburg, Benjamin Recht, and Angjoo Kanazawa. K-planes: Explicit radiance fields in space, time, and appearance. In *Proceedings of the IEEE/CVF Conference on Computer Vision and Pattern Recognition*, pages 12479–12488, 2023. 2, 3, 5
- [8] Hao He, Yinghao Xu, Yuwei Guo, Gordon Wetzstein, Bo Dai, Hongsheng Li, and Ceyuan Yang. Cameractrl: Enabling camera control for text-to-video generation. *arXiv preprint arXiv:2404.02101*, 2024. 3
- [9] Shoukang Hu, Tao Hu, and Ziwei Liu. Gauhuman: Articulated gaussian splatting from monocular human videos. In *Proceedings of the IEEE/CVF conference on computer vision and pattern recognition*, pages 20418–20431, 2024. 2
- [10] Yudong Jin, Sida Peng, Xuan Wang, Tao Xie, Zhen Xu, Yifan Yang, Yujun Shen, Hujun Bao, and Xiaowei Zhou. Dif-fuman4d: 4d consistent human view synthesis from sparse-view videos with spatio-temporal diffusion models. *arXiv preprint arXiv:2507.13344*, 2025. 2
- [11] Xinyi Jing, Tao Yu, Renyuan He, Yu-Kun Lai, and Kun Li. Frnerf: Fusion and regularization fields for dynamic view synthesis. *Computational Visual Media*, 2025. 2

- [12] Jiahui Lei, Yijia Weng, Adam Harley, Leonidas Guibas, and Kostas Daniilidis. Mosca: Dynamic gaussian fusion from casual videos via 4d motion scaffolds. *arXiv preprint arXiv:2405.17421*, 2024. 3
- [13] Tianye Li, Mira Slavcheva, Michael Zollhoefer, Simon Green, Christoph Lassner, Changil Kim, Tanner Schmidt, Steven Lovegrove, Michael Goesele, Richard Newcombe, et al. Neural 3d video synthesis from multi-view video. In *Proceedings of the IEEE/CVF conference on computer vision and pattern recognition*, pages 5521–5531, 2022. 2, 5, 6
- [14] Zhan Li, Zhang Chen, Zhong Li, and Yi Xu. Spacetime gaussian feature splatting for real-time dynamic view synthesis. In *Proceedings of the IEEE/CVF Conference on Computer Vision and Pattern Recognition*, pages 8508–8520, 2024. 2
- [15] Yiming Liang, Tianhan Xu, and Yuta Kikuchi. Himor: Monocular deformable gaussian reconstruction with hierarchical motion representation. In *Proceedings of the Computer Vision and Pattern Recognition Conference*, pages 886–895, 2025. 3
- [16] Youtian Lin, Zuozhuo Dai, Siyu Zhu, and Yao Yao. Gaussian-flow: 4d reconstruction with dynamic 3d gaussian particle. In *Proceedings of the IEEE/CVF Conference on Computer Vision and Pattern Recognition*, pages 21136–21145, 2024. 2
- [17] Fangfu Liu, Diankun Wu, Yi Wei, Yongming Rao, and Yueqi Duan. Sherpa3d: Boosting high-fidelity text-to-3d generation via coarse 3d prior. In *Proceedings of the IEEE/CVF Conference on Computer Vision and Pattern Recognition*, pages 20763–20774, 2024. 3
- [18] Qingming Liu, Yuan Liu, Jiepeng Wang, Xianqiang Lyv, Peng Wang, Wenping Wang, and Junhui Hou. Modgs: Dynamic gaussian splatting from casually-captured monocular videos with depth priors, 2025. 3
- [19] Xiaoxiao Long, Yuan-Chen Guo, Cheng Lin, Yuan Liu, Zhiyang Dou, Lingjie Liu, Yuexin Ma, Song-Hai Zhang, Marc Habermann, Christian Theobalt, et al. Wonder3d: Single image to 3d using cross-domain diffusion. In *Proceedings of the IEEE/CVF conference on computer vision and pattern recognition*, pages 9970–9980, 2024. 3
- [20] Richard A Newcombe, Dieter Fox, and Steven M Seitz. Dynamicfusion: Reconstruction and tracking of non-rigid scenes in real-time. In *Proceedings of the IEEE conference on computer vision and pattern recognition*, pages 343–352, 2015. 1
- [21] Maxime Oquab, Timothée Darcet, Théo Moutakanni, Huy Vo, Marc Szafraniec, Vasil Khalidov, Pierre Fernandez, Daniel Haziza, Francisco Massa, Alaaeldin El-Nouby, et al. Dinov2: Learning robust visual features without supervision. *arXiv preprint arXiv:2304.07193*, 2023. 3
- [22] Jongmin Park, Minh-Quan Viet Bui, Juan Luis Gonzalez Bello, Jaeho Moon, Jihyong Oh, and Munchurl Kim. Splinesg: Robust motion-adaptive spline for real-time dynamic 3d gaussians from monocular video. In *Proceedings of the Computer Vision and Pattern Recognition Conference*, pages 26866–26875, 2025. 3
- [23] Adam Paszke, Sam Gross, Francisco Massa, Adam Lerer, James Bradbury, Gregory Chanan, Trevor Killeen, Zeming Lin, Natalia Gimelshein, Luca Antiga, et al. Pytorch: An imperative style, high-performance deep learning library. *Advances in neural information processing systems*, 32, 2019. 5
- [24] Sida Peng, Junting Dong, Qianqian Wang, Shangzhan Zhang, Qing Shuai, Xiaowei Zhou, and Hujun Bao. Animatable neural radiance fields for modeling dynamic human bodies. In *Proceedings of the IEEE/CVF International Conference on Computer Vision*, pages 14314–14323, 2021. 2
- [25] Sida Peng, Yuanqing Zhang, Yinghao Xu, Qianqian Wang, Qing Shuai, Hujun Bao, and Xiaowei Zhou. Neural body: Implicit neural representations with structured latent codes for novel view synthesis of dynamic humans. In *Proceedings of the IEEE/CVF conference on computer vision and pattern recognition*, pages 9054–9063, 2021. 2
- [26] Neus Sabater, Guillaume Boisson, Benoit Vandame, Paul Kerbiriou, Frederic Babon, Matthieu Hog, Remy Gendrot, Tristan Langlois, Olivier Bureller, Arno Schubert, et al. Dataset and pipeline for multi-view light-field video. In *Proceedings of the IEEE conference on computer vision and pattern recognition Workshops*, pages 30–40, 2017. 2, 5, 6, 7, 8
- [27] Johannes Lutz Schönberger and Jan-Michael Frahm. Structure-from-motion revisited. In *Conference on Computer Vision and Pattern Recognition (CVPR)*, 2016. 5, 6
- [28] Johannes Lutz Schönberger, Enliang Zheng, Marc Pollefeys, and Jan-Michael Frahm. Pixelwise view selection for unstructured multi-view stereo. In *European Conference on Computer Vision (ECCV)*, 2016. 5, 6
- [29] Yichun Shi, Peng Wang, Jianglong Ye, Mai Long, Kejie Li, and Xiao Yang. Mvdream: Multi-view diffusion for 3d generation. *arXiv preprint arXiv:2308.16512*, 2023. 3
- [30] Wenqiang Sun, Shuo Chen, Fangfu Liu, Zilong Chen, Yueqi Duan, Jun Zhang, and Yikai Wang. Dimensionx: Create any 3d and 4d scenes from a single image with controllable video diffusion. *arXiv preprint arXiv:2411.04928*, 2024. 3
- [31] Chaoyang Wang, Ashkan Mirzaei, Vidit Goel, Willi Menapace, Aliaksandr Siarohin, Avalon Vinella, Michael Vasilkovsky, Ivan Skorokhodov, Vladislav Shakhrai, Sergey Korolev, et al. 4real-video-v2: Fused view-time attention and feedforward reconstruction for 4d scene generation. *arXiv preprint arXiv:2506.18839*, 2025. 3
- [32] Qianqian Wang, Vickie Ye, Hang Gao, Jake Austin, Zhengqi Li, and Angjoo Kanazawa. Shape of motion: 4d reconstruction from a single video, 2024. 2, 3
- [33] Zhou Wang, Alan C Bovik, Hamid R Sheikh, and Eero P Simoncelli. Image quality assessment: from error visibility to structural similarity. *IEEE transactions on image processing*, 13(4):600–612, 2004. 5, 7
- [34] Zhouxia Wang, Ziyang Yuan, Xintao Wang, Yaowei Li, Tianshui Chen, Menghan Xia, Ping Luo, and Ying Shan. Motionctrl: A unified and flexible motion controller for video generation. In *ACM SIGGRAPH 2024 Conference Papers*, pages 1–11, 2024. 3
- [35] Zihan Wang, Jeff Tan, Tarasha Khurana, Neehar Peri, and Deva Ramanan. Monofusion: Sparse-view 4d reconstruction via monocular fusion. *arXiv preprint arXiv:2507.23782*, 2025. 2, 3, 6, 7

- [36] Chung-Yi Weng, Brian Curless, Pratul P Srinivasan, Jonathan T Barron, and Ira Kemelmacher-Shlizerman. Humanerf: Free-viewpoint rendering of moving people from monocular video. In *Proceedings of the IEEE/CVF conference on computer vision and pattern Recognition*, pages 16210–16220, 2022. 2
- [37] Diankun Wu, Fangfu Liu, Yi-Hsin Hung, Yue Qian, Xiaohang Zhan, and Yueqi Duan. 4d-fly: Fast 4d reconstruction from a single monocular video. In *Proceedings of the Computer Vision and Pattern Recognition Conference*, pages 16663–16673, 2025. 3
- [38] Guanjun Wu, Taoran Yi, Jiemin Fang, Lingxi Xie, Xiaopeng Zhang, Wei Wei, Wenyu Liu, Qi Tian, and Xinggang Wang. 4d gaussian splatting for real-time dynamic scene rendering. In *Proceedings of the IEEE/CVF conference on computer vision and pattern recognition*, pages 20310–20320, 2024. 2, 3, 6, 7
- [39] Kailu Wu, Fangfu Liu, Zhihan Cai, Runjie Yan, Hanyang Wang, Yating Hu, Yueqi Duan, and Kaisheng Ma. Unique3d: High-quality and efficient 3d mesh generation from a single image. *Advances in Neural Information Processing Systems*, 37:125116–125141, 2024. 3
- [40] Rundi Wu, Ruiqi Gao, Ben Poole, Alex Trevithick, Changxi Zheng, Jonathan T Barron, and Aleksander Holynski. Cat4d: Create anything in 4d with multi-view video diffusion models. In *Proceedings of the Computer Vision and Pattern Recognition Conference*, pages 26057–26068, 2025. 3
- [41] Tong Wu, Yu-Jie Yuan, Ling-Xiao Zhang, Jie Yang, Yan-Pei Cao, Ling-Qi Yan, and Lin Gao. Recent advances in 3d gaussian splatting. *Computational Visual Media*, 10(4):613–642, 2024. 1
- [42] Dejjia Xu, Weili Nie, Chao Liu, Sifei Liu, Jan Kautz, Zhangyang Wang, and Arash Vahdat. Camco: Camera-controllable 3d-consistent image-to-video generation. *arXiv preprint arXiv:2406.02509*, 2024. 3
- [43] Zeyu Yang, Hongye Yang, Zijie Pan, and Li Zhang. Real-time photorealistic dynamic scene representation and rendering with 4d gaussian splatting. *arXiv preprint arXiv:2310.10642*, 2023. 2, 3, 5, 6, 7
- [44] Ziyi Yang, Xinyu Gao, Wen Zhou, Shaohui Jiao, Yuqing Zhang, and Xiaogang Jin. Deformable 3d gaussians for high-fidelity monocular dynamic scene reconstruction. In *Proceedings of the IEEE/CVF conference on computer vision and pattern recognition*, pages 20331–20341, 2024. 2
- [45] Junliang Ye, Fangfu Liu, Qixiu Li, Zhengyi Wang, Yikai Wang, Xinzhou Wang, Yueqi Duan, and Jun Zhu. Dreamreward: Text-to-3d generation with human preference. In *European Conference on Computer Vision*, pages 259–276. Springer, 2024. 3
- [46] Jae Shin Yoon, Kihwan Kim, Orazio Gallo, Hyun Soo Park, and Jan Kautz. Novel view synthesis of dynamic scenes with globally coherent depths from a monocular camera. In *Proceedings of the IEEE/CVF Conference on Computer Vision and Pattern Recognition*, pages 5336–5345, 2020. 2, 5, 6, 7, 8
- [47] Tanveer Younis and Zhanglin Cheng. Sparse-view 3d reconstruction: Recent advances and open challenges, 2025. 2
- [48] Wangbo Yu, Jinbo Xing, Li Yuan, Wenbo Hu, Xiaoyu Li, Zhipeng Huang, Xiangjun Gao, Tien-Tsin Wong, Ying Shan, and Yonghong Tian. Viewcrafter: Taming video diffusion models for high-fidelity novel view synthesis. *arXiv preprint arXiv:2409.02048*, 2024. 2, 3, 5
- [49] Richard Zhang, Phillip Isola, Alexei A Efros, Eli Shechtman, and Oliver Wang. The unreasonable effectiveness of deep features as a perceptual metric. In *Proceedings of the IEEE conference on computer vision and pattern recognition*, pages 586–595, 2018. 5, 7

SparseCam4D: Spatio-Temporally Consistent 4D Reconstruction from Sparse Cameras

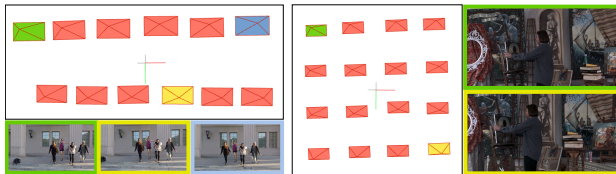
Supplementary Material

6. Implementation Details

Our framework is implemented in PyTorch, using the RealTime4DGS codebase as the foundation. To assess the versatility of our method, we did not apply dataset-specific tuning; instead, a unified training schedule was adopted across all datasets. For the optimization of 4D Gaussians, we strictly follow the official RealTime4DGS implementation. The Adam optimizer is employed throughout. The learning rate for each feature plane starts at 1.6×10^{-3} and exponentially decays to 1.6×10^{-4} . The tiny MLP decoder is trained with an initial learning rate of 1.6×10^{-4} , which decays to 1.6×10^{-5} . In the distortion field, we configure the base resolution of the spatial axes to 64. The basis resolution for temporal axis is set according to the total number of frames in the training sequence, while the pose axis is set to the number of generated views. For the multi-resolution feature structure, we employ a scale factor of 2 for each feature plane. We also find that expanding this factor from 2 to [2,4] will contribute to rendering quality at the expense of higher training cost. To stabilize the optimization process, we introduce a warm-up stage during the first 1000 iterations. In this phase, only the 4D Gaussian primitives are optimized, while both the distortion field and camera pose optimization remain frozen. After this warm-up stage, joint optimization over the distortion field, camera poses, and Gaussian attributes is enabled. This staged training scheme prevents instability in the early iterations and ensures smoother convergence.

6.1. Camera Selection

6.1.1. Training Cameras



(a) Jumping

(b) Painter

Figure 8. **Visualization of selected training cameras.** The non-red frustums denote the cameras used for training, corresponding to the images shown at the bottom and on the right respectively. The remaining red frustums indicate the cameras used for evaluation.

We construct a minimal subset of cameras C_s from the original set C (usually containing 12-21 cameras) to serve as the training views. The subset C_s is required to satisfy

Algorithm 1: Camera Subset Selection with Overlap-Constrained Greedy Expansion

Input:

$P[i]$: Visible point sets for each camera i
 $\text{overlap}[i][j]$: overlap matrix between camera i and camera j , defined as $\text{overlap}[i][j] = \frac{|P_i \cap P_j|}{|P_i \cup P_j|}$

o_{\min} : overlap threshold

τ : target coverage

μ : overlap weight

Output: Selected camera subset for training C_s

```

1 foreach camera  $i$  do
2    $G_{\text{nbr}}[i] \leftarrow \{j \mid \text{overlap}[i][j] \geq o_{\min}, j \neq i\}$ 
3 end
4  $P_{\text{total}} \leftarrow \bigcup_i P[i]$  // all visible points
5  $U \leftarrow P_{\text{total}}$  // uncovered points
6  $c_0 \leftarrow$  top-left camera
7  $C_s \leftarrow \{c_0\}$ 
8  $U \leftarrow U \setminus P[c_0]$ 
9  $c_{\text{cur}} \leftarrow c_0$ 
10 while  $1 - |U|/|P_{\text{total}}| < \tau$  do
11    $\mathcal{N} \leftarrow \{v \in G_{\text{nbr}}[c_{\text{cur}}] \mid v \notin C_s\}$ 
12   if  $\mathcal{N} = \emptyset$  then
13     break
14   end
15   foreach  $v \in \mathcal{N}$  do
16      $\text{gain}(v) \leftarrow |P[v] \cap U|$ 
17      $\text{score}(v) \leftarrow \text{gain}(v) \cdot (1 + \mu \cdot \text{overlap}[c_{\text{cur}}][v])$ 
18   end
19    $v^* \leftarrow \arg \max_{v \in \mathcal{N}} \text{score}(v)$ 
20   if  $|P[v^*] \cap U| = 0$  then
21     break
22   end
23    $C_s \leftarrow C_s \cup \{v^*\}$ 
24    $U \leftarrow U \setminus P[v^*]$ 
25    $c_{\text{cur}} \leftarrow v^*$ 
26 end
27 return  $C_s$ 

```

two conditions: 1) C_s should sufficiently cover the scene content observed by C ; 2) Since VDM will interpolate additional viewpoints within C_s , the per-frame overlap among cameras in C_s is expected to be similar in order to ensure uniform scene coverage. Based on these criteria, we propose a greedy selection strategy that jointly considers visible point coverage and field-of-view overlap. The algorithm begins by choosing the camera located at the top-left



Figure 9. **Reliability of PSNR vs. LPIPS in Ablation Experiments.** We find that directly using generated-view reconstruction introduces severe oversmoothness that, paradoxically, favors PSNR computation, preventing PSNR from accurately reflecting changes in reconstruction quality. In contrast, LPIPS effectively captures the variations in reconstruction quality under these ablation settings.

position as the starting view. At each iteration, we construct a set of candidate cameras whose overlap with the current camera exceeds the minimum adjacency threshold o_{min} . For each candidate v , we compute a score that balances newly covered points and the geometric consistency with the current camera:

$$\text{score}(v) = |P[v] \cap U| \cdot (1 + \mu \cdot \text{overlap}[c_{cur}, v]), \quad (11)$$

where U denotes the set of currently uncovered points and $\mu = 0.05$ is the overlap weight. The first term encourages maximal expansion of scene coverage, while the second ensures that consecutive selected cameras maintain sufficient overlap for reliable view interpolation using generative models. The candidate with the highest score is added to the selected subset, and the uncovered set is updated accordingly. The process iterates until the target coverage ratio is achieved or no valid candidates remain, yielding the final camera subset. We summarize the details in Algorithm 1. Tab. 10-12 provides camera index references for training and evaluation. Fig. 8 illustrates the selected training cameras from two example scenes *Jumping* and *Painter*, with the training cameras highlighted in different colors.

6.1.2. Evaluation Cameras

To fully reflect the rendering quality of each method under the sparse-view setting, we do not adopt the original approach of evaluation using only one single selected camera. Instead, evaluation is performed on all remaining cameras.

7. Metrics selection in Ablation Study

In the ablation study, SSIM and LPIPS are adopted as the primary evaluation metrics instead of PSNR. This choice is motivated by two considerations. First, SSIM and LPIPS are more sensitive to structural details, with LPIPS in particular capturing perceptual differences in texture, sharpness, and local geometry, whereas PSNR primarily reflects pixel-wise color discrepancies and is less aligned with perceptual

image quality. Second, as illustrated in Fig. 9, the rendered images produced without distortion field exhibit substantial generative inconsistency, leading to overly smooth and blurred outputs. Such behavior tends to favor PSNR, resulting in only a marginal difference. In contrast, SSIM and LPIPS, especially LPIPS, capture the degradation of structural fidelity and perceptual quality, revealing the significant discrepancy.

8. Additional Evaluation Results

8.1. Evaluation under Different Sparsity Levels.

We compare our method with the baseline 4DGS approach, *i.e.* 4DGaussian, under different sparsity levels, and the results are reported in Tab. 5. Our method outperforms the baseline across all camera-view configurations, further demonstrating its practical robustness.

Table 5. **Performance with different number of camera views.** We set 4DGaussian as the baseline model for dynamic scene reconstruction and evaluate the rendering quality with different number of training views.

	3 views			6 views			9 views		
	PSNR \uparrow	SSIM \uparrow	LPIPS \downarrow	PSNR \uparrow	SSIM \uparrow	LPIPS \downarrow	PSNR \uparrow	SSIM \uparrow	LPIPS \downarrow
4DGaussian	16.72	0.435	0.546	19.86	0.581	0.448	21.41	0.601	0.430
Ours	21.56	0.656	0.264	23.58	0.687	0.243	24.72	0.751	0.205

8.2. Efficiency Comparison with RealTime4DGS

Since our implementation is based on the RealTime4DGS codebase, we compare our method against it in terms of rendering fps to further evaluate efficiency. As shown in Tab 6, our approach maintains the similar rendering speed as RealTime4DGS. Notably, the proposed distortion field is discarded after training, so inference complexity remains comparable to RealTime4DGS.

8.3. Per-scene Breakdown Results

In Tab. 8, Tab. 7, and Tab. 9, we provide a breakdown of the metrics for different scenes in the Neural 3D Video, Tech-

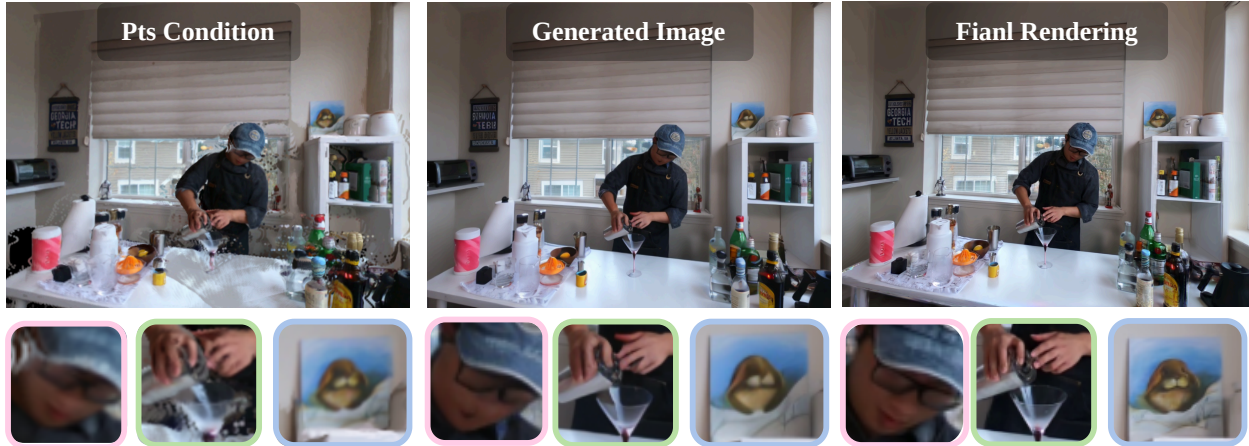


Figure 10. Visualization of the point-cloud rendering condition, generation prior, and final results.

Table 6. Efficiency Comparison with RealTime4DGS.

	Coffee Martini	Playground	Average
RealTime4DGS	11.48fps	11.51fps	11.50fps
Ours	11.82fps	11.97fps	11.90fps

nicolor, and Nvidia Dynamic Scenes datasets, respectively. As shown in the quantitative results, our method demonstrates clear superiority over the other five approaches. This indicates that our method effectively leverages the generated priors while mitigating the inconsistency they may introduce. In addition, since our evaluation is conducted on all cameras excluding those used for training, we provide more detailed per-camera metrics, as reported in Tab. 10-12.

8.4. Additional Qualitative Results

In Fig. 13, Fig. 14-17, and Fig. 19, 18, we showcase additional rendering comparisons with those methods aforementioned at different timesteps. Our method consistently recovers high-quality and coherent renderings over time, demonstrating its effectiveness in dynamic scenes with sparse observation. Please zoom in for more details.

9. More Details for Generated Images

In our main experiments, we adopt ViewCrafter to provide additional observations, from which 20–25 generated views are uniformly sampled for training. ViewCrafter conditions its diffusion model on point-cloud renderings obtained from Dust3R, given two input images along with the target trajectory. However, we find that the quality of generated images is highly dependent on the quality of the point-cloud renderings. To improve the generation quality, we replace Dust3r with a stronger 3D foundation model, VGGT, to produce more reliable conditioning signals. Despite this improvement, the generated sequences still exhibit spatio-temporal inconsistencies that hinder their direct use for 4D reconstruction, as illustrated in Fig 10. Such inconsistencies can

lead to severe over-blurring in the reconstructed results, as shown in Fig. 9 (right).

As for the ablation study with ReCamMaster, unlike ViewCrafter, which leverages point-cloud renderings as trajectory priors, ReCamMaster directly conditions on camera parameters to generate a video sequence of 81 frames. Without explicit geometric constraints, the generated images from vanilla ReCamMaster suffer from severe hallucinations, making them unsuitable for reconstruction. To address this, we finetune ReCamMaster by incorporating point-cloud renderings as an additional conditioning signal, analogous to ViewCrafter.

9.1. Failure Case

Although our method substantially mitigates the inter-frame inconsistencies caused by distortions in generated images, the final performance still partially depends on the quality of the generated images themselves. As illustrated in Fig. 11, when the generated images are of poor quality—typically due to out-of-domain inputs or generative hallucinations—such as the severely deformed human body and the additional ghosting artifacts shown in the figure, addressing only the inter-image inconsistency is insufficient to achieve satisfactory reconstruction results. Without considering training cost, incorporating the generative model into the reconstruction pipeline for joint or iterative optimization is a promising direction for future exploration.

10. More visualization

To gain an intuitive understanding of the STDF training results, we visualize the full feature maps (16 channels) of each plane in the CoffeeMartini scene in Fig. 12. The activated regions vary across different dimensions, indicating the intertwined nature of spatial and temporal deformations.

To further interpret the outputs, we render the deformation predictions of STDF as an additional attribute field. This allows us to clearly observe the regions in the scene



Figure 11. **Visualization of one failure case.** From left to right are the source image and point-cloud-rendering condition provided to ViewCrafter, the corresponding generated image, and a Gaussian rendering near that generated image. Since ViewCrafter is primarily trained on scene-centric data with few human subjects, this example suffers from an out-of-domain issue. In addition, the quality of the point-cloud-rendering condition is relatively low. These factors jointly lead to low-quality generated images, which in turn degrade the Gaussian reconstruction quality on the human body.

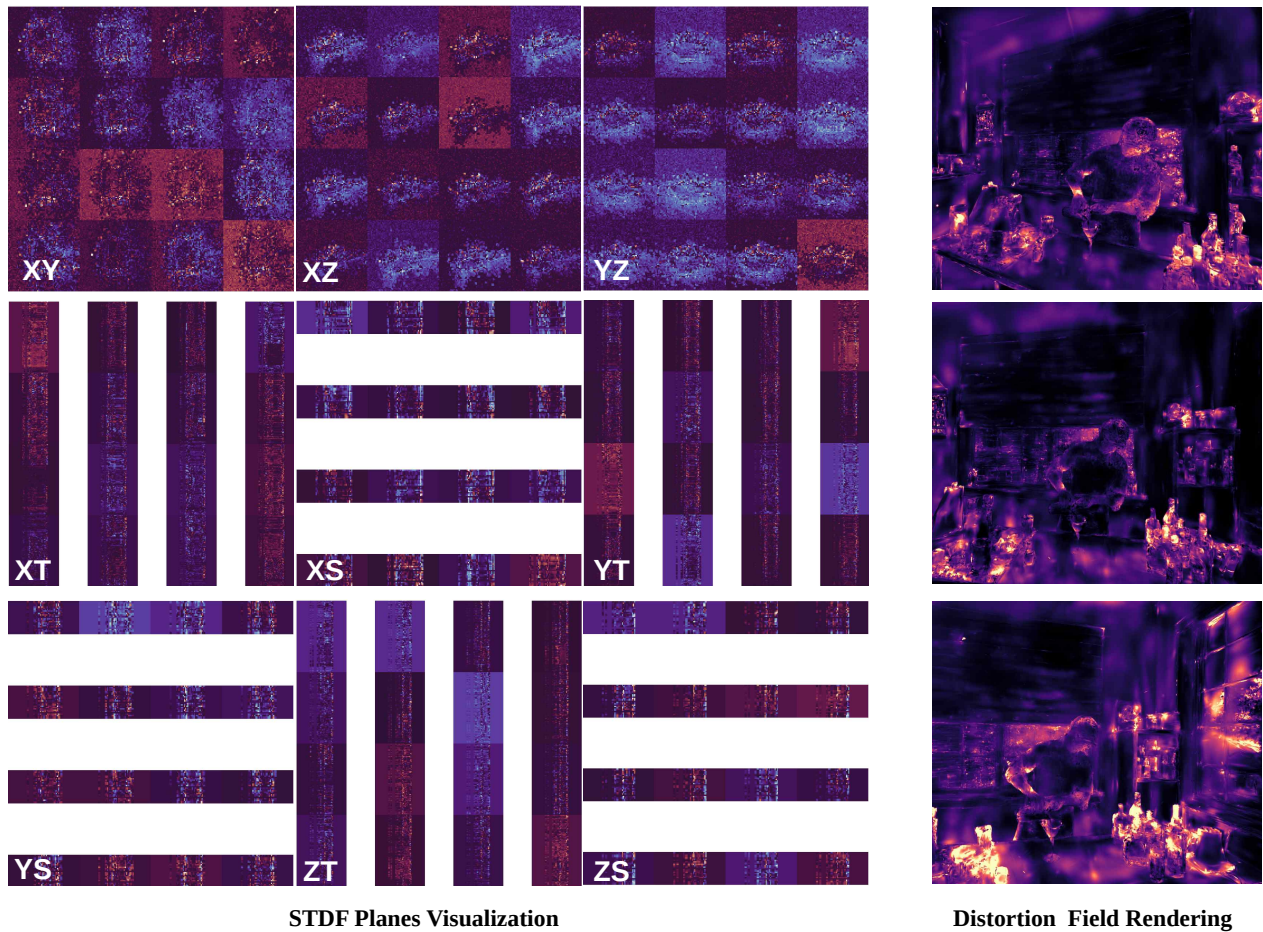


Figure 12. Visualization of Spatio-Temporal Distortion Field

where distortions occur. Through this visualization approach, we can intuitively perceive the spatio-temporal distortions present in the 4D scene.

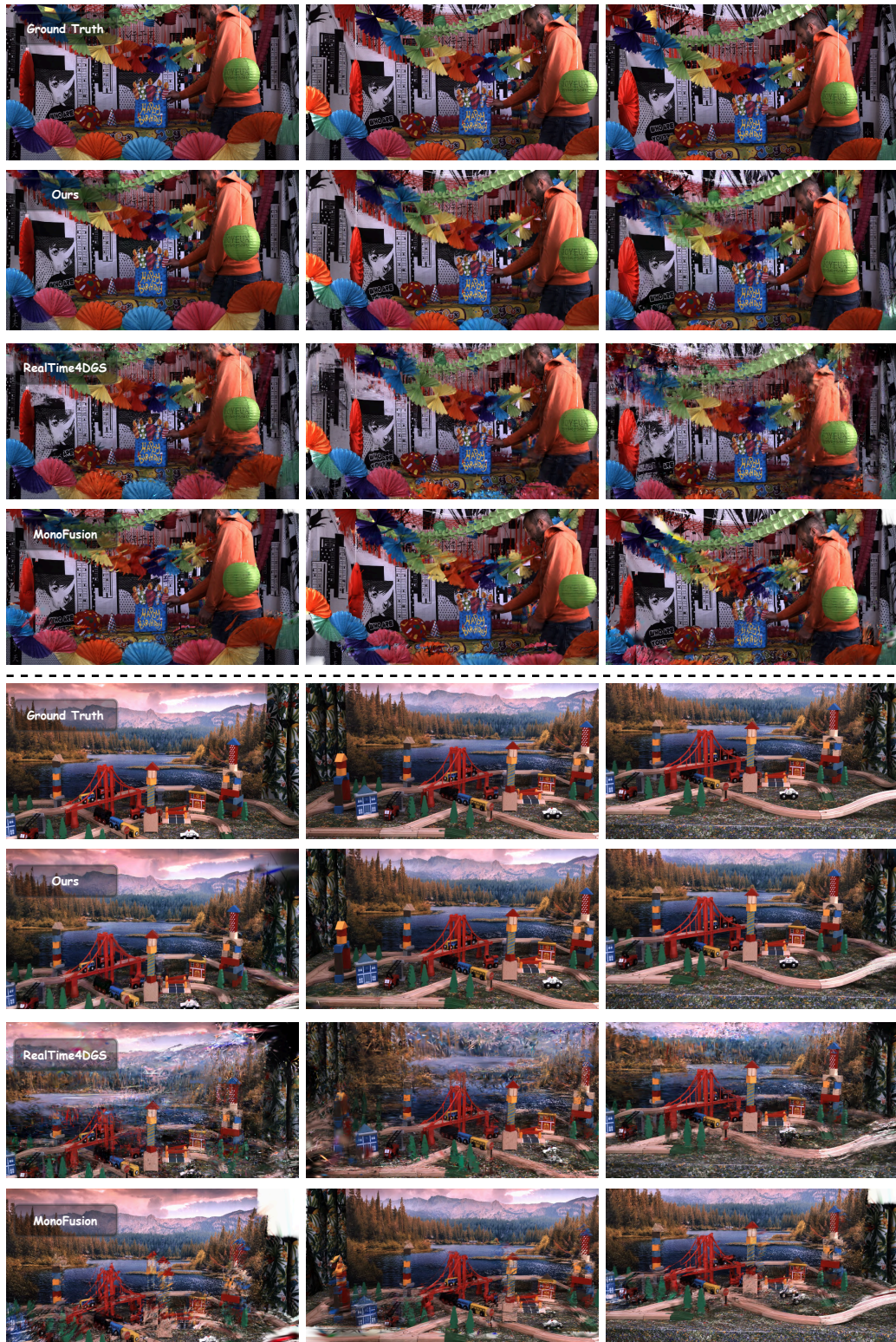


Figure 13. **Additional qualitative comparison results on *Technicolor* Dataset.** We highlight the geometric completeness of background structures, bottom decorations, and the red bridge across different viewpoints, as well as the temporal consistency of dynamic regions such as human faces, the ‘Happy Birthday’ text, and the toy train.



Figure 14. Additional qualitative comparison results on *Neural 3D Video Dataset* (part I).



Figure 15. Additional qualitative comparison results on *Neural 3D Video Dataset (part II)*.

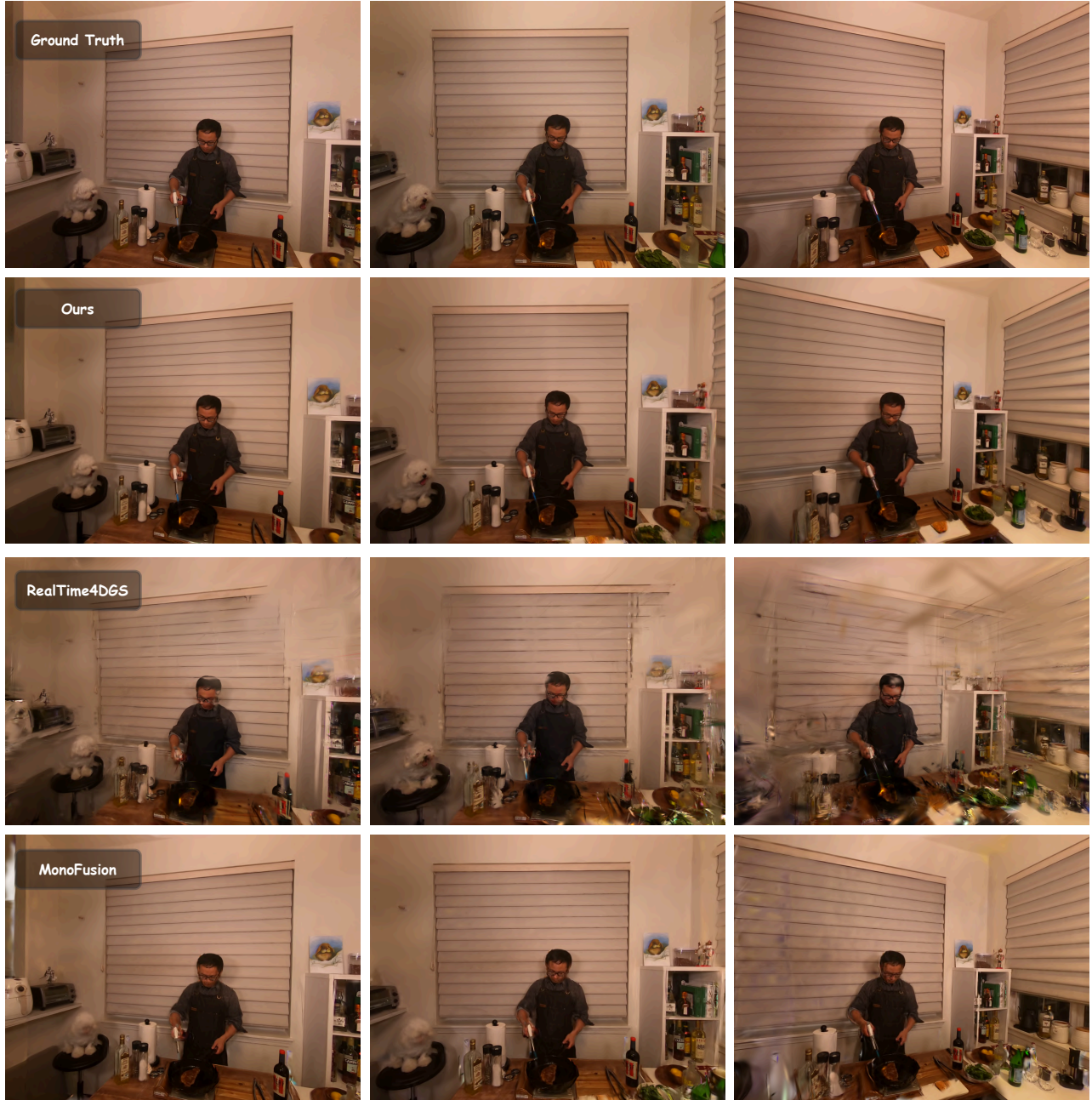


Figure 16. Additional qualitative comparison results on *Neural 3D Video Dataset* (part III).

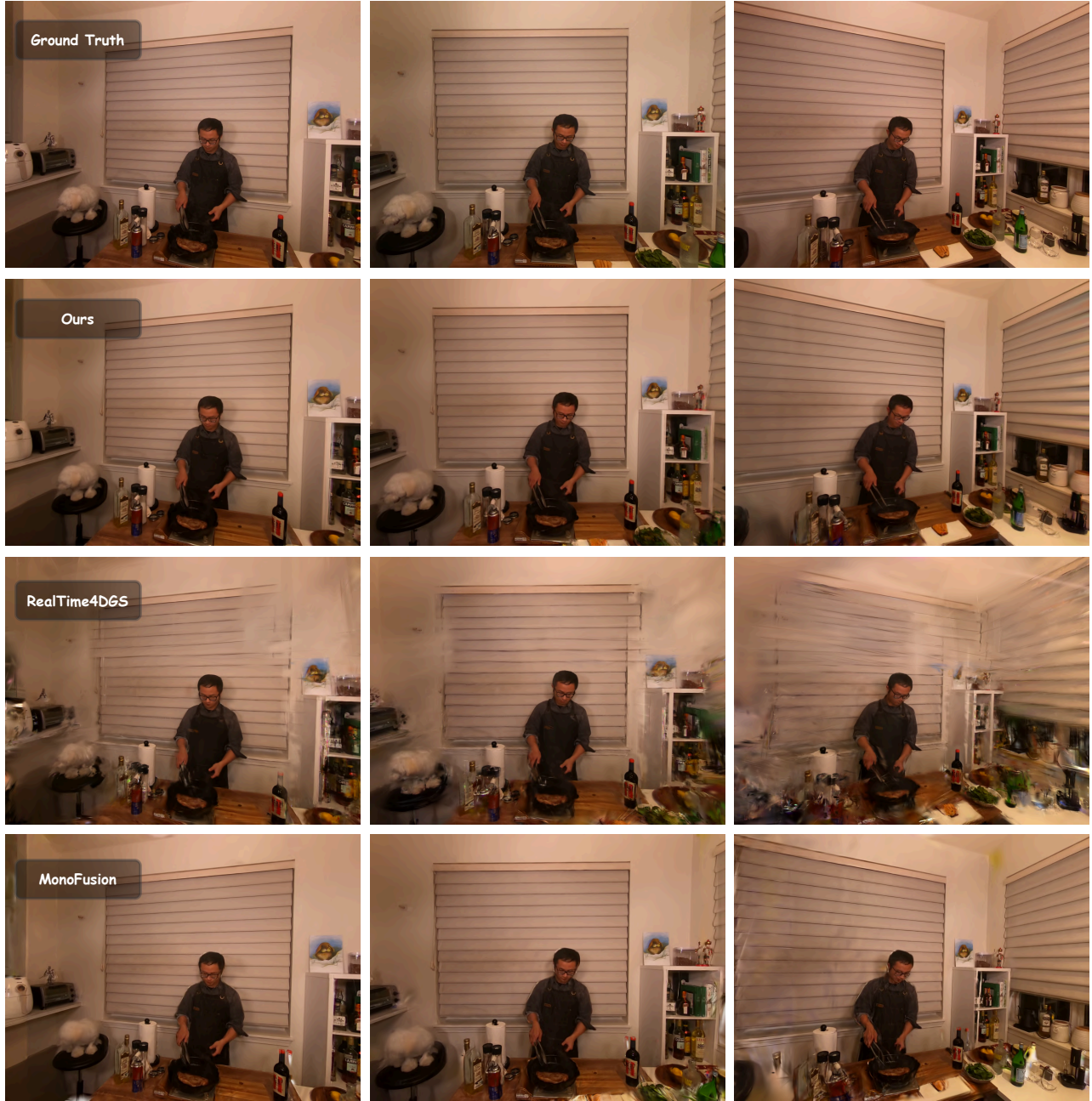


Figure 17. Additional qualitative comparison results on *Neural 3D Video Dataset* (part IV).

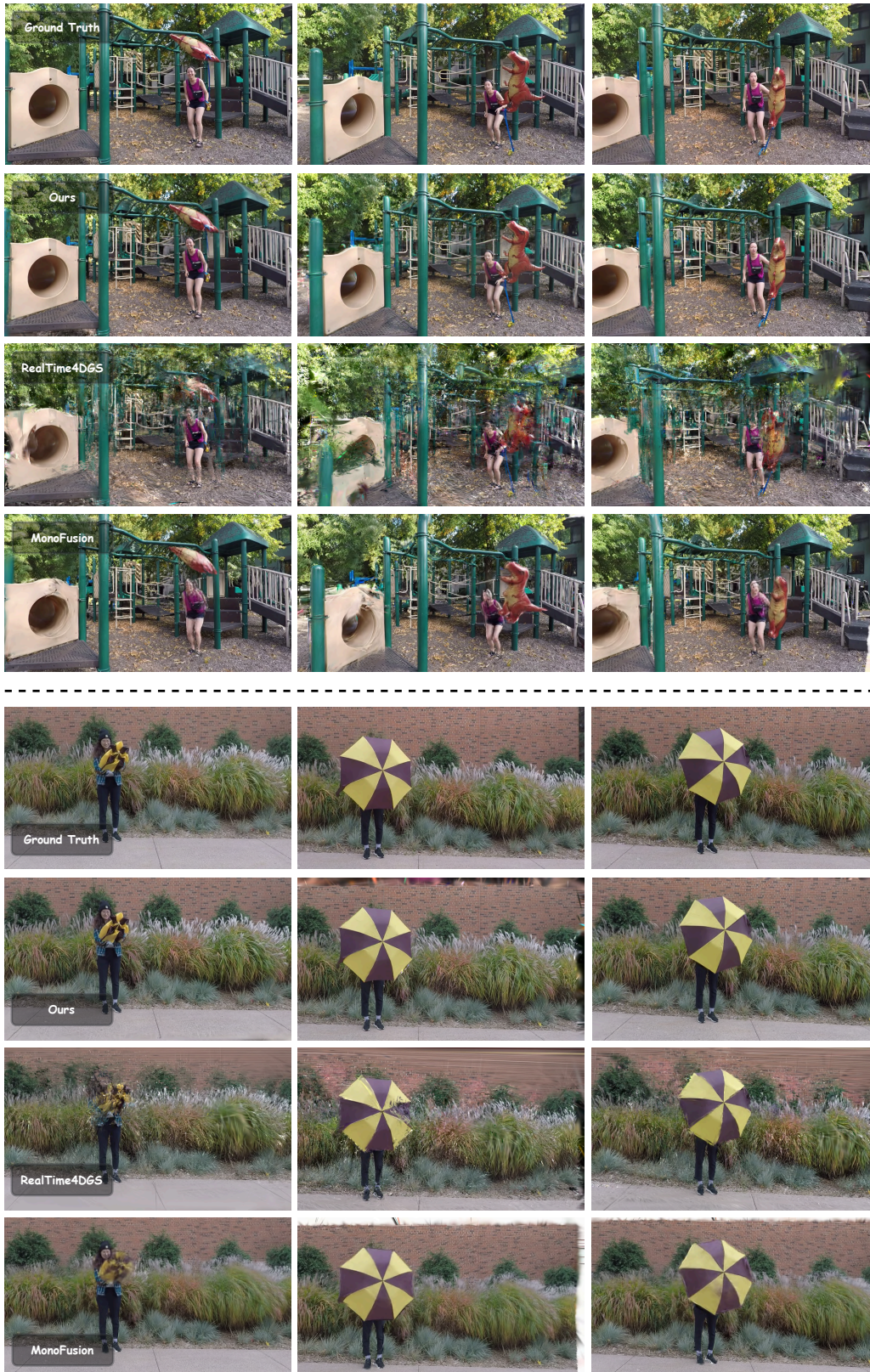


Figure 18. **Additional qualitative comparison results on *Nvidia Dynamic Scenes Dataset (part I)*.** In the top panel, we emphasize the geometric completeness of the left archway and the right escalator across different viewpoints, as well as the temporal consistency of dynamic regions such as the human body, balloon, and the blue tether. In the bottom panel, we highlight the fine details of background grass, shoes, and umbrella textures, together with accurate motion fitting under fast movement in the leftmost column.



Figure 19. Additional qualitative comparison results on *Nvidia Dynamic Scenes Dataset* (part II).

Table 7. PSNR, SSIM, and LPIPS of our framework on Technicolor, with cam00, cam09 and cam15 served as training views.

Technicolor - PSNR						
	Fabien	Theater	Train	Birthday	Painter	Average
HyperReel	13.62	14.24	15.44	12.28	15.13	14.14
4DGaussians	18.31	17.53	16.72	11.97	16.48	16.20
4DRotor	15.21	16.00	14.01	12.42	16.62	14.85
RealTime4DGS	13.00	16.27	16.59	18.45	18.76	16.53
MonoFusion	17.86	19.48	15.12	16.47	20.92	17.97
Ours	25.23	22.44	21.56	20.11	26.39	23.15

Technicolor - SSIM						
	Fabien	Theater	Train	Birthday	Painter	Average
HyperReel	0.653	0.434	0.351	0.341	0.484	0.453
4DGaussians	0.704	0.552	0.435	0.335	0.499	0.505
4DRotor	0.625	0.479	0.270	0.307	0.450	0.426
RealTime4DGS	0.520	0.451	0.438	0.586	0.556	0.510
MonoFusion	0.737	0.590	0.392	0.524	0.648	0.578
Ours	0.814	0.686	0.656	0.683	0.802	0.728

Technicolor - LPIPS						
	Fabien	Theater	Train	Birthday	Painter	Average
HyperReel	0.514	0.666	0.595	0.664	0.642	0.616
4DGaussians	0.492	0.539	0.546	0.620	0.564	0.552
4DRotor	0.574	0.571	0.589	0.612	0.560	0.581
RealTime4DGS	0.614	0.623	0.505	0.437	0.529	0.542
MonoFusion	0.415	0.380	0.356	0.339	0.271	0.352
Ours	0.340	0.379	0.264	0.274	0.236	0.299

Table 8. PSNR, SSIM, and LPIPS of our framework on Neural 3D Video, with cam01, cam05 and cam10 served as training views.

Neural 3D Video - PSNR							
	coffee martini	cook spinach	cut roasted beef	flame salmon	flame steak	sear steak	Average
HyperReel	14.07	16.44	17.04	10.64	17.57	17.28	15.63
4DGaussians	14.49	17.94	18.34	14.83	19.53	18.57	17.40
4DRotor	15.86	19.65	18.51	16.10	19.69	19.05	18.20
RealTime4DGS	15.07	17.95	17.04	14.65	19.57	18.86	17.31
MonoFusion	15.59	19.71	19.15	15.42	20.02	19.91	18.43
Ours	18.40	23.93	22.43	18.92	23.30	23.56	21.91

Neural 3D Video - SSIM							
	coffee martini	cook spinach	cut roasted beef	flame salmon	flame steak	sear steak	Average
HyperReel	0.520	0.586	0.635	0.452	0.644	0.633	0.582
4DGaussian	0.593	0.664	0.696	0.611	0.736	0.716	0.673
4DRotor	0.649	0.741	0.715	0.651	0.753	0.744	0.708
RealTime4DGS	0.590	0.670	0.640	0.569	0.708	0.700	0.649
MonoFusion	0.643	0.780	0.777	0.630	0.788	0.784	0.738
Ours	0.729	0.832	0.792	0.726	0.820	0.818	0.789

Neural 3D Video - LPIPS							
	coffee martini	cook spinach	cut roasted beef	flame salmon	flame steak	sear steak	Average
HyperReel	0.540	0.499	0.447	0.604	0.466	0.459	0.500
4DGaussians	0.401	0.320	0.325	0.362	0.258	0.270	0.320
4DRotor	0.406	0.334	0.359	0.371	0.334	0.336	0.357
RealTime4DGS	0.471	0.428	0.459	0.485	0.405	0.412	0.442
MonoFusion	0.367	0.228	0.236	0.354	0.229	0.231	0.270
Ours	0.298	0.232	0.259	0.291	0.237	0.238	0.258

Table 9. PSNR, SSIM, and LPIPS of our framework on Nvidia Dynamic Scenes, with cam01, cam06 and cam10 as training views.

Nvidia Dynamic Scenes - PSNR							
	jumping	balloon1	balloon3	playground	skating	umbrella	Average
HyperReel	24.45	15.46	22.58	15.41	21.05	24.74	19.88
4DGaussians	17.38	16.96	14.56	12.75	19.70	19.52	16.81
4DRotor	21.90	14.55	20.33	10.95	26.28	22.29	19.38
RealTime4DGS	17.85	18.36	19.07	13.96	18.52	19.71	17.91
MonoFusion	20.72	20.31	19.81	16.86	23.55	20.07	20.22
Ours	24.36	25.31	25.33	19.64	28.73	25.42	24.81

Nvidia Dynamic Scenes - SSIM							
	jumping	balloon1	balloon3	playground	skating	umbrella	Average
HyperReel	0.782	0.350	0.632	0.281	0.669	0.629	0.528
4DGaussians	0.525	0.372	0.264	0.166	0.607	0.299	0.372
4DRotor	0.731	0.311	0.497	0.137	0.814	0.556	0.508
RealTime4DGS	0.585	0.533	0.509	0.267	0.649	0.333	0.479
MonoFusion	0.687	0.563	0.542	0.499	0.819	0.428	0.590
Ours	0.793	0.810	0.791	0.672	0.906	0.794	0.794

Nvidia Dynamic Scenes - LPIPS							
	jumping	balloon1	balloon3	playground	skating	umbrella	Average
HyperReel	0.256	0.537	0.266	0.491	0.450	0.238	0.396
4DGaussians	0.454	0.473	0.609	0.608	0.449	0.498	0.516
4DRotor	0.245	0.601	0.392	0.670	0.166	0.260	0.389
RealTime4DGS	0.450	0.371	0.380	0.499	0.422	0.432	0.426
MonoFusion	0.241	0.151	0.174	0.206	0.134	0.248	0.192
Ours	0.170	0.127	0.142	0.190	0.121	0.148	0.150

Table 10. PSNR, SSIM, and LPIPS of our framework on **Technicolor**. Three cameras (cam00, cam09 and cam15) are served as training views for scene *Fabien*, *Theater* and *Train*, while only two cameras (cam00 and cam15) are training views for scene *Birthday* and *Painter*.

Technicolor - PSNR						
	Fabien	Theater	Train	Birthday	Painter	Average
cam01	25.581	21.231	23.456	19.562	26.322	23.23
cam02	21.886	19.203	21.202	18.227	25.736	21.251
cam03	18.844	18.5	19.468	17.692	27.939	20.488
cam04	28.676	23.089	23.59	20.991	27.423	24.754
cam05	28.162	23.422	23.833	20.837	27.249	24.701
cam06	23.838	20.949	21.0	19.824	25.58	22.238
cam07	20.735	19.916	19.228	19.306	25.717	20.98
cam08	28.175	23.997	23.649	20.245	25.817	24.377
cam10	25.706	23.722	20.932	20.962	26.613	23.587
cam11	24.939	23.549	21.013	21.682	27.519	23.741
cam12	25.122	23.568	20.321	19.482	23.795	22.457
cam13	27.505	25.954	21.626	20.643	26.436	24.433
cam14	28.818	24.666	20.962	21.986	26.913	24.669
Average	25.23	22.444	21.56	20.111	26.389	23.147

Technicolor - SSIM						
	Fabien	Theater	Train	Birthday	Painter	Average
cam01	0.846	0.665	0.71	0.69	0.789	0.74
cam02	0.801	0.609	0.638	0.634	0.803	0.697
cam03	0.75	0.556	0.644	0.651	0.86	0.692
cam04	0.835	0.697	0.726	0.715	0.823	0.759
cam05	0.842	0.755	0.762	0.709	0.824	0.779
cam06	0.821	0.675	0.658	0.682	0.784	0.724
cam07	0.776	0.62	0.619	0.675	0.761	0.69
cam08	0.81	0.725	0.741	0.683	0.787	0.749
cam10	0.825	0.701	0.539	0.687	0.797	0.71
cam11	0.82	0.687	0.665	0.726	0.826	0.745
cam12	0.778	0.689	0.562	0.64	0.761	0.686
cam13	0.83	0.781	0.657	0.669	0.819	0.751
cam14	0.85	0.753	0.612	0.713	0.79	0.744
Average	0.814	0.686	0.656	0.683	0.802	0.728

Technicolor - LPIPS						
	Fabien	Theater	Train	Birthday	Painter	Average
cam01	0.305	0.355	0.24	0.245	0.218	0.273
cam02	0.355	0.431	0.301	0.303	0.231	0.324
cam03	0.394	0.484	0.328	0.319	0.218	0.349
cam04	0.34	0.342	0.225	0.24	0.218	0.273
cam05	0.323	0.329	0.214	0.253	0.221	0.268
cam06	0.333	0.399	0.27	0.275	0.235	0.302
cam07	0.367	0.447	0.307	0.291	0.266	0.336
cam08	0.357	0.343	0.211	0.281	0.249	0.288
cam10	0.307	0.36	0.266	0.259	0.24	0.287
cam11	0.304	0.38	0.249	0.235	0.225	0.278
cam12	0.404	0.387	0.315	0.323	0.266	0.339
cam13	0.336	0.316	0.258	0.295	0.247	0.29
cam14	0.287	0.347	0.255	0.241	0.238	0.274
Average	0.34	0.379	0.264	0.274	0.236	0.299

Table 11. PSNR, SSIM, and LPIPS of our framework on **Neural 3D Video**. Three cameras (cam01, cam05 and cam10) are training views.

Neural 3D Video - PSNR							
	coffee martini	cook spinach	cut roasted beef	flame salmon	flame steak	sear steak	Average
cam00	21.654	28.114	26.901	22.323	27.558	27.744	25.715
cam02	25.236	25.926	25.206	24.866	25.472	25.365	25.345
cam03	-	25.194	24.231	-	25.489	25.891	25.201
cam04	25.477	31.417	-	25.741	31.034	30.641	28.862
cam06	20.31	27.966	26.145	21.048	27.624	27.609	25.117
cam07	19.602	26.638	24.25	20.449	25.344	25.759	23.674
cam08	19.134	26.957	24.089	19.889	26.177	26.647	23.816
cam09	20.957	26.997	26.072	21.31	27.161	27.446	24.99
cam11	14.669	20.251	19.145	15.398	19.277	19.349	18.015
cam12	13.623	19.353	18.495	14.841	18.082	18.604	17.166
cam13	15.547	20.289	20.071	16.839	19.371	20.014	18.688
cam14	16.705	22.012	22.252	17.309	20.462	21.098	19.973
cam15	-	22.182	21.68	16.824	20.618	21.2	20.501
cam16	15.457	21.483	20.783	16.689	20.086	20.699	19.199
cam17	-	22.11	20.975	-	20.894	21.646	21.406
cam18	14.762	21.959	20.944	15.755	20.997	21.37	19.298
cam19	17.115	22.534	21.444	17.245	22.972	23.031	20.722
cam20	15.736	19.319	18.569	16.248	20.715	20.014	18.434
Average	18.399	23.927	22.426	18.923	23.296	23.563	21.905

Neural 3D Video - SSIM							
	coffee martini	cook spinach	cut roasted beef	flame salmon	flame steak	sear steak	Average
cam00	0.832	0.907	0.897	0.841	0.918	0.915	0.885
cam02	0.875	0.917	0.906	0.87	0.907	0.905	0.897
cam03	-	0.919	0.893	-	0.903	0.911	0.906
cam04	0.889	0.941	-	0.884	0.945	0.94	0.92
cam06	0.767	0.898	0.862	0.774	0.899	0.894	0.849
cam07	0.735	0.876	0.814	0.754	0.859	0.861	0.816
cam08	0.735	0.874	0.8	0.754	0.874	0.87	0.818
cam09	0.786	0.892	0.868	0.8	0.893	0.892	0.855
cam11	0.673	0.751	0.712	0.643	0.735	0.723	0.706
cam12	0.65	0.717	0.684	0.627	0.689	0.69	0.676
cam13	0.67	0.772	0.76	0.676	0.756	0.753	0.731
cam14	0.726	0.815	0.804	0.719	0.792	0.787	0.774
cam15	-	0.797	0.772	0.691	0.779	0.774	0.762
cam16	0.669	0.772	0.74	0.676	0.744	0.746	0.724
cam17	-	0.772	0.728	-	0.741	0.752	0.748
cam18	0.613	0.767	0.716	0.629	0.739	0.732	0.699
cam19	0.667	0.785	0.758	0.656	0.79	0.792	0.741
cam20	0.646	0.795	0.757	0.62	0.799	0.787	0.734
Average	0.729	0.832	0.792	0.726	0.82	0.818	0.789

Neural 3D Video - LPIPS							
	coffee martini	cook spinach	cut roasted beef	flame salmon	flame steak	sear steak	Average
cam00	0.21	0.173	0.185	0.195	0.167	0.17	0.183
cam02	0.184	0.16	0.173	0.179	0.169	0.17	0.172
cam03	-	0.169	0.186	-	0.179	0.177	0.178
cam04	0.181	0.155	-	0.17	0.151	0.151	0.161
cam06	0.25	0.183	0.207	0.235	0.179	0.182	0.206
cam07	0.273	0.183	0.223	0.252	0.191	0.192	0.219
cam08	0.266	0.182	0.222	0.249	0.178	0.18	0.213
cam09	0.219	0.15	0.168	0.204	0.146	0.147	0.172
cam11	0.37	0.317	0.339	0.372	0.326	0.329	0.342
cam12	0.388	0.324	0.346	0.387	0.344	0.343	0.355
cam13	0.358	0.281	0.291	0.347	0.286	0.292	0.309
cam14	0.313	0.252	0.261	0.312	0.259	0.264	0.277
cam15	-	0.265	0.285	0.327	0.271	0.276	0.284
cam16	0.357	0.278	0.304	0.345	0.294	0.293	0.312
cam17	-	0.274	0.308	-	0.291	0.288	0.29
cam18	0.384	0.278	0.311	0.372	0.291	0.296	0.322
cam19	0.352	0.277	0.294	0.348	0.268	0.27	0.301
cam20	0.373	0.279	0.307	0.367	0.27	0.272	0.311
Average	0.298	0.232	0.259	0.291	0.237	0.238	0.258

Table 12. **PSNR, SSIM, and LPIPS of our framework on Nvidia Dynamic Scenes.** Three cameras (cam01, cam06 and cam10) are training views.

Nvidia Dynamic Scenes - PSNR							
	jumping	balloon1	balloon3	playground	skating	umbrella	Average
cam02	25.867	26.076	28.318	19.736	32.098	26.946	26.507
cam03	23.858	25.564	27.681	19.201	26.698	27.409	25.069
cam04	25.41	25.337	26.352	18.441	30.907	27.033	25.58
cam05	26.698	26.248	27.455	20.261	32.017	28.36	26.84
cam07	24.477	25.839	27.519	19.161	29.468	22.384	24.808
cam08	25.006	24.963	21.572	19.643	30.531	22.493	24.035
cam09	27.679	27.486	23.516	19.941	33.348	23.373	25.89
cam11	20.699	25.297	24.761	20.925	21.651	25.361	23.116
cam12	19.521	20.987	20.808	19.436	21.827	25.385	21.328
Average	24.357	25.311	25.331	19.638	28.727	25.416	24.807

Nvidia Dynamic Scenes - SSIM							
	jumping	balloon1	balloon3	playground	skating	umbrella	Average
cam02	0.818	0.848	0.878	0.695	0.93	0.822	0.832
cam03	0.756	0.82	0.88	0.626	0.826	0.818	0.788
cam04	0.802	0.814	0.845	0.617	0.908	0.807	0.799
cam05	0.858	0.845	0.832	0.699	0.934	0.84	0.835
cam07	0.78	0.83	0.848	0.625	0.919	0.758	0.793
cam08	0.814	0.795	0.519	0.67	0.931	0.686	0.736
cam09	0.875	0.87	0.81	0.69	0.949	0.8	0.832
cam11	0.784	0.836	0.805	0.74	0.894	0.813	0.812
cam12	0.65	0.635	0.699	0.684	0.865	0.799	0.722
Average	0.793	0.81	0.791	0.672	0.906	0.794	0.794

Nvidia Dynamic Scenes - LPIPS							
	jumping	balloon1	balloon3	playground	skating	umbrella	Average
cam02	0.144	0.108	0.106	0.182	0.096	0.122	0.126
cam03	0.197	0.12	0.108	0.187	0.156	0.147	0.152
cam04	0.165	0.128	0.119	0.23	0.113	0.139	0.149
cam05	0.127	0.115	0.115	0.177	0.094	0.129	0.126
cam07	0.176	0.126	0.12	0.219	0.13	0.178	0.158
cam08	0.159	0.134	0.216	0.197	0.113	0.175	0.166
cam09	0.128	0.106	0.153	0.176	0.097	0.161	0.137
cam11	0.185	0.126	0.143	0.151	0.138	0.137	0.147
cam12	0.248	0.182	0.195	0.192	0.152	0.148	0.186
Average	0.17	0.127	0.142	0.19	0.121	0.148	0.15